

THE EVOLUTION OF RADIO GALAXIES AND X-RAY POINT SOURCES IN COMA CLUSTER PROGENITORS SINCE $Z \sim 1.2$

QUYEN N. HART¹, JOHN T. STOCKE¹, AUGUST E. EVRARD², ERICA E. ELLINGSON¹, AND WAYNE A. BARKHOUSE³

ACCEPTED FOR PUBLICATION IN THE ASTROPHYSICAL JOURNAL: July 8, 2011

ABSTRACT

Using *Chandra* imaging spectroscopy and Very Large Array (VLA) L-band radio maps, we have identified radio sources at $P_{1.4GHz} \geq 5 \times 10^{23} \text{ W Hz}^{-1}$ and X-ray point sources (XPSs) at $L_{0.3-8keV} \geq 5 \times 10^{42} \text{ erg s}^{-1}$ in $L > L^*$ galaxies in 12 high-redshift ($0.4 < z < 1.2$) clusters of galaxies. The radio galaxies and XPSs in this cluster sample, chosen to be consistent with Coma Cluster progenitors at these redshifts, are compared to those found at low- z analyzed in Hart et al. (2009). Within a projected radius of 1 Mpc of the cluster cores, we find 17 cluster radio galaxies (11 with secure redshifts, including one luminous FR II radio source at $z=0.826$, and 6 more with host galaxy colors similar to cluster ellipticals). The radio luminosity function (RLF) of the cluster radio galaxies as a fraction of the cluster red sequence (CRS) galaxies reveals significant evolution of this population from high- z to low- z , with higher power radio galaxies situated in lower temperature clusters at earlier epochs. Additionally, there is some evidence that cluster radio galaxies become more centrally concentrated than CRS galaxies with cosmic time. Within this same projected radius, we identify 7 spectroscopically-confirmed cluster XPSs, all with CRS host galaxy colors. Consistent with the results from Martini et al. (2009), we estimate a minimum X-ray active fraction of $1.4 \pm 0.8\%$ for CRS galaxies in high- z clusters, corresponding to an approximate 10-fold increase from $0.15 \pm 0.15\%$ at low- z . Although complete redshift information is lacking for several XPSs in $z > 0.4$ cluster fields, the increased numbers and luminosities of the CRS radio galaxies and XPSs suggest a substantial (9-10 fold) increase in the heat injected into high redshift clusters by AGN compared to the present epoch.

Subject headings: galaxies: active – galaxies: clusters: general – radio continuum: galaxies – X-rays: galaxies: clusters – X-rays: galaxies

1. INTRODUCTION

Clusters of galaxies are special environments in which to study the evolution of galaxies and active galactic nuclei (AGN) because these massive structures contain a hot, diffuse intracluster medium (ICM) that is detectable in the X-ray. The disturbed appearance of extended radio emission from individual cluster galaxies (e.g., NGC 1265 in the Perseus cluster; O’Dea & Owen 1986) was the first indication that an ICM existed (e.g., Miley et al. 1972) and early X-ray observations detected it at $T=10^7-8 \text{ K}$ (Sarazin 1986, and references therein). With the high-resolution of the *Chandra* Advanced CCD Imaging Spectrometer (ACIS), it was found that the radio-lobes of nearby AGN in the brightest cluster galaxy (BCG) appear to be coincident with cavities in X-ray surface brightness (e.g., Perseus cluster; Fabian et al. 2002). The physical connection suggested by this spatial coincidence allows an indirect measurement of the kinetic power produced by these AGN.

The connection between AGN and galaxy evolution is not well-understood, but theoretical results suggest that the absence of extremely massive galaxies is due to the truncation of star formation (e.g., Bell et al. 2004). AGN

have been implicated as the mechanism to “shut-off” star-formation by heating the surrounding gas and/or ejecting the gas reservoirs necessary for galaxy growth during outburst episodes (e.g., Bower et al. 2006). Heating by AGN has also been suggested to account for anomalies in the scaling relationship between cluster X-ray luminosity and temperature (Borgani et al. 2004, and references therein). Particularly in low-mass clusters (i.e., clusters with low X-ray temperatures), an “entropy” floor is observed; Ponman et al. (1999) suggest that pre-heating of the ICM is required to explain this feature. This entropy floor may be due to the heat injection by AGN in these clusters over time.

In general the X-ray surface brightness of a cluster ICM is well-fit by a β -model, which is similar to a King profile. However, some clusters display a strong peak of X-ray emission at their centers. Assuming that thermal bremsstrahlung is the dominant cooling process in cluster cores, the cooling time for the X-ray emitting gas is shorter than the Hubble time in these “cool-core clusters”. Therefore, prodigious amounts of star formation ($\geq 100 \text{ M}_\odot/\text{year}$) are expected; however, spectroscopic X-ray observations fail to detect line emission from this gas at $kT < 1 \text{ keV}$ (Peterson et al. 2003), nor do optical observations reveal significant amounts of star formation (e.g., McNamara & O’Connell 1989, 1993). The lack of strong evidence for wide-spread star formation in cluster cores suggests that a source of heat is preventing the ICM from cooling in cluster cores. AGN are likely contributors to “feedback” processes that are required to prevent this large-scale cooling.

¹ Center for Astrophysics and Space Astronomy, Department of Astrophysical and Planetary Sciences, UCB-389, University of Colorado, Boulder, CO 80309, USA

² Departments of Physics and Astronomy and Michigan Center for Theoretical Physics, University of Michigan, Ann Arbor, MI 48109-1040, USA

³ (For the ChaMP collaboration) Department of Physics and Astrophysics, University of North Dakota, Grand Forks, ND 58202, USA

The connection between AGN and their surrounding environments, both small and large, proves to be a difficult problem to simulate. Many cosmological simulations are large volume boxes in which computational efficiency is balanced by the need to resolve small structures, such as galaxies, and to track cluster scale-properties that are several orders of magnitudes larger than galaxies. Thus, in practice, some cosmological simulations inject a pre-determined amount of “heat” at the centers of evolving clusters to simulate pre-heating of the cluster cores. Hydrodynamical simulations of the plasma-filled lobes created by the AGN in cluster BCGs can recreate the observed X-ray structures (e.g., Ruszkowski et al. 2004) and halt the formation of strong cool-core clusters; however, these simulations in general cannot efficiently distribute the heat throughout the cluster core (e.g., Vernaleo & Reynolds 2007). One potential solution to this difficulty is that more than just the one AGN in the BCG contribute to heating the ICM.

Previous studies have found statistical excesses of radio galaxies (e.g., Lin & Mohr 2007) and X-ray point sources, or XPSs, in the vicinity of galaxy clusters (e.g., Ruderman & Ebeling 2005; Cappelluti et al. 2005). The higher surface density of AGN in and around clusters brings up some interesting questions: (1) Is the enhanced surface density simply a direct result of a higher density of galaxies? (2) Are cluster AGN triggered into activity as they pass through the dense cluster cores? (3) Is the cluster environment especially suited in some specific way to create AGN activity? Radio galaxies and XPSs are clearly associated with AGN activity at the core of their host galaxies. In order to consistently study cluster AGN, observations obtained in at least three wavelength regimes are required to detect these objects and to understand the energy feedback processes between them and the surrounding ICM.

In Hart et al. (2009), hereafter Paper I, we examined the cluster radio galaxy and XPS population in eleven $0.2 < z < 0.4$ clusters. Within 1 Mpc from the cluster center, we detected 20 radio galaxies at $P_{1.4GHz} \geq 3 \times 10^{23}$ W Hz⁻¹ and 8 XPSs at $L_{0.3-8.0keV} \geq 10^{42}$ erg s⁻¹, all spectroscopically-confirmed as cluster members with host galaxies at $L \geq L^*$. These cluster sources are hosted by cluster “red sequence” (CRS) ellipticals, but are more centrally concentrated than the CRS galaxies as a whole. The cluster XPSs in our low- z cluster sample show little evidence for obscuration based both on their optical colors, which are consistent with the CRS, and also on the absence of significant obscuration in the X-ray. Based on the optical and X-ray properties of these cluster XPSs, we suggested that these sources are most similar to low-luminosity, high-energy peaked BL Lacertae (BL Lac) objects. Based on the extrapolations of the radio luminosity function (RLF) of radio galaxies and the X-ray luminosity function (XLF) of BL Lacs to lower radio and X-ray luminosities, we estimate that almost all CRS galaxies are radio-loud at $P_{1.4GHz} \geq 10^{21.4}$ W Hz⁻¹ and X-ray-loud at $L_{0.3-8.0keV} \geq 10^{40}$ erg s⁻¹. Therefore, most CRS galaxies possess AGN jets which can deposit heat into the ICM as they move through the inner cluster regions.

Paper I concluded that the radio-loud CRS population between $10^{21.4} < P_{1.4GHz} < 10^{23.5}$ W Hz⁻¹ can inject $\sim 55\%$ of the total energy to the ICM if we assume a shal-

low scaling law of AGN jet power to radio luminosity, namely $P_{jet} \propto L_r^{0.5}$ from Birzan et al. (2008). More recently Cavagnolo et al. (2010) extended the Birzan et al. (2008) sample to lower-power radio galaxies and measured a steeper slope for this scaling relationship ($P_{jet} \propto L_r^{0.7}$), which decreases the estimated heat input by low-luminosity AGN to 30%. In Paper I the number of confirmed cluster radio galaxies is much larger than cluster XPSs and so cluster radio galaxies will dominate the ICM heating regardless of the interpretation of XPSs.

In this paper, we continue our study of cluster AGN begun in Paper I with the goal of studying the evolution of radio galaxies and XPSs in galaxy clusters. We examine twelve $0.4 < z < 1.2$ clusters to detect radio galaxies at $P_{1.4GHz} \geq 5 \times 10^{23}$ W Hz⁻¹ and XPSs at $L_{0.3-8.0keV} \geq 5 \times 10^{42}$ erg s⁻¹ within a 1 Mpc projected radius of the cluster cores to determine the distribution of AGN luminosities, their locations relative to the ICM, and their numbers and luminosities as a function of redshift. In §2 we describe the cosmological simulations that guide the selection of our cluster sample, uniquely designed to permit an accurate evolutionary study. In §3, we detail the X-ray, radio, and optical datasets used to measure the ICM X-ray temperatures, to identify potential cluster XPSs and radio sources, and to obtain optical colors of typical cluster galaxies and AGN host galaxies. In §4 we present the sample of potential cluster radio galaxies and XPSs, summarize their optical properties through composite color-magnitude diagrams, and describe the typical colors of cluster radio galaxies and XPSs relative to the CRS. In §5–6 we present the RLF of cluster radio galaxies out to $z=1.1$ and compare it to other cluster RLFs. In §7 we examine the XPS population in our cluster fields out to $z=1.2$ to determine if any statistical XPS excess above the expected background is observed and estimate the X-ray active fraction of CRS galaxies. In §8 we discuss our results and in §9 we summarize our conclusions from this study. X-ray luminosities are defined for the rest-frame (0.3–8.0 keV) bandpass, unless otherwise noted. Radio powers are defined for a 1.4 GHz rest-frame frequency. Throughout this paper, we use $H_0 = 70$ km s⁻¹ Mpc⁻¹, $\Omega_\Lambda = 0.70$, and $\Omega_M = 0.3$.

2. THE “ROAD TO COMA” CLUSTER SAMPLE

Hierarchical structure formation predicts that the highest density fluctuations in the primordial universe grow and assemble into the large galaxy clusters in the present epoch (Peacock 1999). As clusters accrete gas and galaxies, the cluster dark matter halos increase in mass. The evolution of such massive structures has been simulated (e.g., Evrard et al. 2002; Millennium Simulation, Springel et al. 2005; ENZO simulations, Hallman et al. 2007; Nagai et al. 2007) to follow the physics of the intracluster gas, to predict cluster observables, and to suggest the need for AGN feedback.

In particular, AGN feedback is difficult to simulate in large-scale cosmological simulations because of the unknown range of AGN powers and duty cycles, energy transport mechanisms through the ICM, and feedback processes within the host galaxies themselves and their surrounding environment (e.g., Bower et al. 2006, and references therein). Recent simulations of AGN feedback in galaxy cluster environments include the evolution of

over-pressurized “bubbles” in the ICM, presumably inflated by the radio-emitting lobes associated with the radio-loud AGN in the BCG (e.g., Brüggén et al. 2005, 2009). These simulations successfully recreate X-ray features observed in nearby clusters like the Perseus cluster (Fabian et al. 2002). Other numerical approaches include detailed AGN jet simulations of radio sources both at the cluster center and moving through the ICM (e.g., Heinz et al. 2006; O’Neill & Jones 2010). Observational details of the radio galaxy population is crucial to compile AGN-related input parameters that can be utilized in these large-scale cosmological simulations.

Observationally, X-ray surveys of galaxy clusters (e.g., *Einstein* Extended Medium Sensitivity Survey (EMSS), Gioia & Luppino 1994; Wide Angle ROSAT Pointed Survey (WARPS), Perlman et al. 2002; Massive Cluster Survey (MACS), Ebeling et al. 2001; ROSAT Deep Cluster Survey (RDCS), Rosati et al. 1998) are flux-limited surveys that preferentially select X-ray luminous (and thus high mass) galaxy clusters at high- z . Additionally, depending on the selection method used to identify the extended emission of the ICM, these surveys also tend to identify clusters with centrally peaked X-ray emission typically associated with cool-core clusters (specifically the EMSS; Pesce et al. 1990; Lewis et al. 2002). Therefore, comparisons using flux-limited samples may significantly bias cluster evolutionary studies.

Simulations of cluster evolution indicate that, while clusters experience a variety of formation histories, the mean progenitor mass increases with time in a regular manner (Wechsler et al. 2002). Evolutionary studies in galaxy clusters can be improved by choosing clusters that are statistically likely to evolve into a particular system at low redshift. This approach reduces the inherent bias in choosing luminous X-ray-selected clusters from flux-limited surveys at high- z and using their galaxy and AGN content to compare to clusters at low- z . Thus, to minimize the potential biases present in many sample selections, we utilize the results of cosmological simulations from Bialek et al. (2001) to select galaxy clusters at different redshifts, which permit a consistent study of the evolution of galaxies or AGN within these dense environments.

The details of the numerical nature of the cosmological simulations can be found in Bialek et al. (2001), but we summarize the major points here. Smooth particle hydrodynamics (SPH) and N-body codes are incorporated into a Lagrangian code P3MSPH (Evrard 1988) to track the gaseous components, as well as the collisionless particles (i.e., dark matter) in these simulations. These simulations use a standard Λ CDM cosmology with $\Omega_M = 0.3$, $\Omega_\Lambda = 0.7$, $\sigma_8 = 1.0$ and $h = 0.8$, where the Hubble constant, H , is defined as $100 h \text{ km s}^{-1} \text{ Mpc}^{-1}$ and σ_8 is the normalization of the matter power spectrum on $8 h^{-1} \text{ Mpc}$ scales. The simulations were run in a box $300 h^{-1} \text{ Mpc}$ on a side and the most massive cluster dark matter halos ($M > 10^{15} M_\odot$) were tracked throughout the simulation. To match the observed scaling laws of cluster X-ray temperatures and luminosities, which deviate from the expected scaling due to pure gravitational collapse models, these gaseous components are “preheated” by specifying an initial hot temperature for the baryons at earlier epochs (Bialek et al. 2001).

Sixty-eight massive cluster halos chosen from these

large N-body simulations were re-simulated with gas dynamics on a higher resolution grid. Emission-weighted temperatures of their ICM were extracted at various epochs (T_z) and then compared to their ICM temperatures at the current epoch (T_0) in the simulation. We identify Coma Cluster progenitors between $0.2 < z < 1.2$ in the following manner. Using the results of the Bialek et al. (2001) simulations above, the ratio of T_z/T_0 for the fifteen most massive ($M > 10^{15} M_\odot$) cluster halos as a function of redshift is normalized to the bulk ICM temperature of the present-day Coma Cluster ($kT = 8.2 \pm 0.2$; Lutovinov et al. 2008). Figure 1 displays the median temperature of these simulated progenitors as a function of redshift (solid line) and the 25th and 75th percentiles about this distribution (dashed lines). At $z = 0.3$, the median ICM temperature of a Coma Cluster progenitor is predicted to be $7.0 \pm 2.6 \text{ keV}$. The temperature spread reflects the variation in the formation histories of Coma Cluster mass-scale objects in these simulations. At $z = 1.0$, the permitted temperature range for our sample slowly decreases to $4.0 \pm 2.0 \text{ keV}$.

We identify potential “Road to Coma” clusters as having bulk ICM X-ray temperatures that fall within the temperature distribution displayed in Figure 1. Observationally, nearly all cool-core clusters (Burns 1990) host luminous radio sources in their BCGs. Therefore, their exclusion in any cluster sample would decrease the numbers of luminous radio galaxies. In the future this selection method could be improved by using only those simulated clusters which do *not* develop cool cores in the current epoch to better match the Coma Cluster.

The Coma Cluster (or Abell 1656) is a prototypical massive cluster in the present-epoch at $z = 0.023$, with two central dominant galaxies (NGC 4874 and NGC 4889) and a galaxy population dominated by passive ellipticals and S0s. XMM-Newton observations of the Coma Cluster out to the virial radius do not reveal any strong XPSs with $L_{0.5-2.0 \text{ keV}} > 10^{41} \text{ erg s}^{-1}$ (Finoguenov et al. 2004). For an off-center region 1 Mpc from the cluster core, Hornschemeier et al. (2006) did not detect sources with $L_{0.5-8.0 \text{ keV}} > 10^{41} \text{ erg s}^{-1}$ either and report that the number of detected XPSs is consistent with the background estimates. NGC 4874, the western-most central dominant galaxy is detected at $P_{1.4 \text{ GHz}} = 2.4 \times 10^{23} \text{ W Hz}^{-1}$ and NGC 4869, part of an in-falling group to the southwest of NGC 4874, is also detected at $P_{1.4 \text{ GHz}} = 4.8 \times 10^{23} \text{ W Hz}^{-1}$ (Miller et al. 2009). Thus, even for this nearby, massive prototypical cluster, the Coma Cluster does not host powerful radio sources at $P_{1.4 \text{ GHz}} > 10^{24} \text{ W Hz}^{-1}$, nor XPSs at $L_{0.3-8.0 \text{ keV}} > 10^{42} \text{ erg s}^{-1}$. In Paper I, we detected 20 radio galaxies at $P_{1.4 \text{ GHz}} \geq 3 \times 10^{23} \text{ W Hz}^{-1}$ and 8 XPSs at $L_{0.3-8.0 \text{ keV}} \geq 10^{42} \text{ erg s}^{-1}$, yielding 1.8 ± 0.5 radio galaxies and 0.7 ± 0.4 XPSs per cluster. Therefore, detections of two radio galaxies and no XPSs in the Coma Cluster at these power levels are consistent with the expectations based on our previous low- z work in Paper I.

Table 1 lists the full “Road to Coma” cluster sample between $0.2 < z < 1.2$ that is displayed in Figure 1. We broadly define three redshift bins that are used throughout this paper (summarized in Columns 1–2 of Table 1). The low- z redshift bin includes eleven clusters between $0.2 < z < 0.4$, and has been presented and detailed in Paper

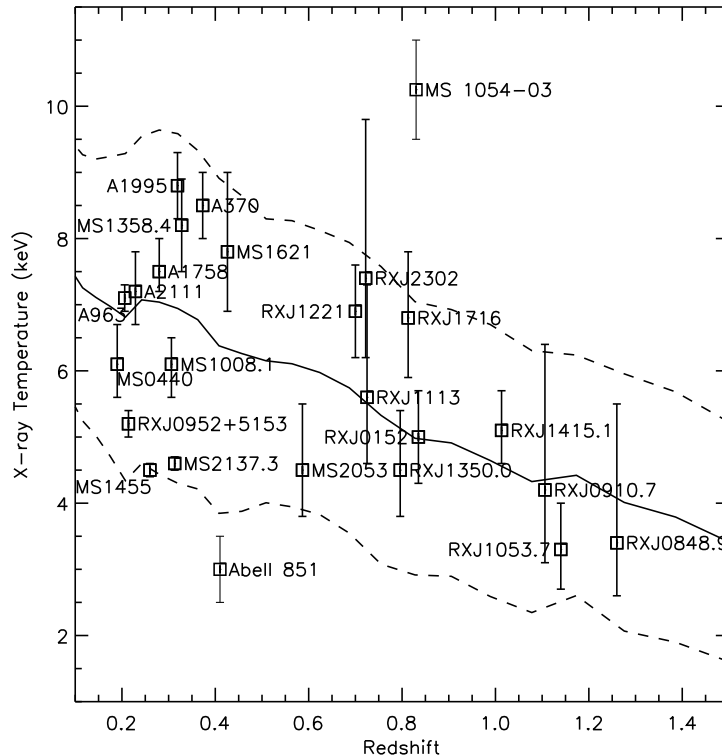


FIG. 1.— Predicted ICM temperature versus redshift of Coma Cluster progenitors. The simulated ICM temperatures of massive cluster halos are tracked in cosmological simulations. For each cluster halo, the ratio of T_z/T_0 is normalized to the current ICM temperature of the Coma Cluster. The mean value of T_z is displayed as the solid line, while the 25th and 75th percentiles of that mean are displayed as dashed-lines. There are eleven clusters between $0.2 < z < 0.4$ that comprise the low- z cluster sample of Paper I. The remaining twelve clusters between $0.4 < z < 1.2$ are the high- z sample discussed in this current study. At the present epoch the Coma Cluster X-ray temperature is 8.2 keV (Lutovinov et al. 2008). Note that the x-axis begins at $z=0.1$ and not $z=0$.

I. The mid- z redshift bin includes five clusters between $0.4 < z < 0.8$, while the high- z redshift bin includes seven clusters between $0.8 < z < 1.2$. Columns 3–5 of Table 1 list the clusters, redshifts, and ICM bulk X-ray temperatures plotted in Figure 1, respectively. The details of the X-ray temperature determinations, measured so as to match most closely the temperatures determined in the simulations, are described in §3.1. Hereafter, we shorten the names of clusters to the first several letters and first four numbers of the full cluster name when referencing them throughout the text.

Note that Abell 851, a well-studied, optically-selected galaxy cluster at $z=0.41$, is well below the “Road to Coma” ($kT=2.9^{+1.3}_{-0.8}$ keV; Schindler & Wambsganss 1996) and is predicted to evolve into a cluster of lower mass compared to the Coma Cluster. Abell 851 has a large blue, star-forming galaxy fraction (Dressler et al. 1994). A rapid evolution (\sim few Gyr) of the blue galaxy population in Abell 851 must take place to be consistent with the galaxy population of Coma-like clusters in the current epoch. However, when the star-forming galaxy population of Abell 851 is compared with the Virgo Cluster, very little evolution in the galaxy population is required. On the other-hand, MS 1054-03 ($z=0.83$) lies well above the “Road to Coma” and it is predicted to evolve into a cluster much more massive than Coma. Therefore, evolutionary studies that utilize MS1054 as a

proto-typical cluster at high- z can be skewed in the opposite direction; e.g., MS1054 has an early-type galaxy fraction similar to the Coma Cluster, suggesting little evolution in galaxy types (Holden et al. 2006) between $z=0.8$ and the present epoch. It is clear that the picture of cluster galaxy evolution looks very different if one chooses Abell 851 or MS1054 to compare against the Coma Cluster. These two examples provide anecdotal evidence supporting our selection procedure.

3. MULTIWAVELENGTH OBSERVATIONS

3.1. *Chandra* Imaging Spectroscopy

Archival *Chandra* observations of the twelve $0.4 < z < 1.2$ clusters in our sample were re-processed using CIAO version 4.1.2 and CALDB 4.1.3. These clusters have published bulk ICM temperatures that fall along the “Road to Coma” in Figure 1. Between $z=0.4$ and $z=1.2$, a circular region within a 1 Mpc projected radius of the cluster center covers between 40% and 20% of one ACIS chip, respectively. For this redshift range, the extended emission of the ICM falls on the ACIS-I3 chip, except for RXJ0849 and RXJ1053, which fall on the ACIS-I2 and ACIS-S3 chips, respectively. We followed the typical pipeline processing of event-1 files by removing bad pixels, afterglow pixels, and streaking patterns. The most recent calibration files for charge transfer inefficiency and time-dependent gain were also applied. The final event

file was filtered on event status and grade. Time periods with background count rates $>3\sigma$ above the observed mean were flagged and removed from further analysis.

Low-resolution ICM spectra were extracted from regions within 1 Mpc (projected) radius from the cluster X-ray emission centroid, except for six $z > 0.8$ clusters where the ICM spectra were extracted from within 500 kpc. (The BCG is identified as the brightest galaxy located closest to the X-ray emission centroid.) These extraction radii were chosen to be as large as possible based on photon statistics in order to compare them with the temperatures derived from the simulations. Background spectra from within an equivalent extraction radius were obtained from the same chip as the cluster detection or on one of the adjacent ACIS chips. The ICM spectra were binned to have a minimum of 20 counts per bin, then modeled using XSPEC (Pratt et al. 2007) with the MEKAL model, foreground extinction held fixed at the Galactic hydrogen column at the cluster location (Dickey & Lockman 1990), and a constant 0.3 solar metal abundance. Column 4 of Table 1 lists the modeled temperatures with 1σ error bars. To identify the cluster X-ray emission centroid, the ICM emission is modeled with a 2-dimensional Gaussian profile. This centroid is identified as the cluster center and a region within 1 Mpc of this center is our analysis region.

We used the CIAO routine *wavdetect*⁴, a detection routine that correlates each image with a Mexican-hat wavelet at different pixel scales (1 to 16) to identify the XPSs in the *Chandra* observations. In our cluster fields at $z > 0.4$, the maximum off-axis angle location for a *wavdetect* source is 4–5' with a minimum source count of 5–9. Kim et al. (2007a) performed extensive simulations on the detection probability of *wavdetect* selection of point sources in *Chandra* ACIS observations. Because the PSF increases in size with increasing off-axis angle from the aimpoint of the *Chandra* observations, these authors simulated sources with counts between 3 and 3000, placed them 0–8' from the aimpoint, and ran *wavdetect* with the *sigthresh* parameter set to 1×10^{-6} . In 2' square images containing simulated sources that incorporated the different parameter space above, Kim et al. (2007a) report a false detection rate of $\sim 1\%$ overall. Referring to Figure 13 in Kim et al. (2007a), the false detection rate is $< 0.8\%$ for sources $< 5'$ from the aimpoint and $< 1.7\%$ for a minimum source count of 5. Therefore, we expect only a small fraction of the *wavdetect* sources found by us to be spurious, or “false”, detections.

Each *wavdetect* source identification was inspected to check source authenticity. Total broadband counts (0.3–8.0 keV) were extracted within a 95% encircled energy radius estimated for a monochromatic energy source of 1.5 keV at the observed off-axis angle⁵. Background counts were extracted within 2–3 times the source extraction radius. XSPEC MEKAL modeling of a typical power-law spectrum with $\Gamma = 1.7$ ($N_E \propto E^{-\Gamma}$) was employed to convert source net counts to unabsorbed X-ray flux. Table 2 lists the X-ray observations for our $z > 0.4$ clusters, including coordinates of the ICM emission centroid (i.e., the “cluster center”), the *Chandra* observation ID,

the ACIS chip with the ICM detection, and the cleansed exposure time. Column 7 of Table 2 lists the estimated flux limit for each observation, determined as the flux of an XPS located 1 Mpc from the cluster center with a count rate 3σ above the background noise. Column 8 of Table 2 is the K-corrected X-ray luminosity limit of an XPS at the cluster redshift (K-correction assumes a power-law spectrum with $\Gamma = 1.7$). Note that we include RXJ0152 here for completeness, although this cluster is not included in the XPS statistics later in this paper because the XPS limiting luminosity of the available *Chandra* images is $\geq 5.0 \times 10^{42}$ erg s⁻¹.

The limiting X-ray luminosities detected in our low- z cluster sample from Paper I is $L_{0.3-8.0\text{keV}} \geq 10^{42}$ erg s⁻¹. Due to the prohibitively long exposure times required to detect equally luminous XPSs at high- z , there are few deep archival *Chandra* cluster observations at $z > 0.8$ that have published temperatures identifying them as Coma Cluster progenitors. As a result the archival *Chandra* images do not uniformly reach down to the same limiting luminosity of $\sim 10^{42}$ erg s⁻¹. The limiting X-ray luminosity limit for our mid- z clusters is 2.2×10^{42} erg s⁻¹ and 5.0×10^{42} erg s⁻¹ for our $0.8 < z < 1.2$ cluster sample, or roughly a factor of 2 increase from one redshift bin to the next. In order to compare our high- z cluster XPSs to the mid- z and low- z cluster XPSs, the X-ray luminosity limit across the entire sample is set at 5.0×10^{42} erg s⁻¹. We note that after we apply a luminosity cut at this value, the minimum source counts range from 9–30 counts in eleven of twelve $0.8 < z < 1.2$ cluster fields listed in Table 2 (excludes RXJ0152). This corresponds to a false detection probability between 0.5–1.5%. We detect 86 XPSs in these 11 fields, of which < 2 sources are expected to be false detections. Given that only a few percent of the < 1 Mpc field-of-view (FOV) of our analysis falls within 5'' of a $\geq L^*$ galaxy (at the cluster redshift), we expect no “false positives” in our final XPS sample.

3.2. Radio Imaging

In September/December 2006 we obtained Very Large Array (VLA) continuum observations at 1.4 GHz (50 MHz bandwidth) for five clusters (RXJ1221, RXJ1113, RXJ1350, RXJ1716, and RXJ0910 under VLA Program AS873). RXJ1221, RXJ1350 and RXJ1716 were observed for 2 hours each in B-array, RXJ1113 for 3.25 hours in BnA-array, and RXJ0910 was observed for 8 hours in B-array. The duration of a typical target scan was 15 minutes, bracketed by 1 minute scans of a nearby phase calibrator. A flux calibrator (e.g., 3C286) was observed for 3 minutes at the beginning and the end of each observing session. We used the National Radio Astronomy Observatory (NRAO)⁶ Astronomical Imaging Processing System (AIPS), version 31DEC09, in the usual manner to flag, calibrate, transform, and clean the images, so that radio sources could be detected manually. Source flux densities are estimated with the AIPS tasks TVWIN and IMEAN. The typical 3σ limit of these observations is 0.1–0.2 mJy.

The 1.4 GHz radio maps and source identifications for

⁴ <http://cxc.harvard.edu/ciao/ahelp/wavdetect.html>

⁵ http://cxc.harvard.edu/cal/Hrma/psf/ECF/hrmaD1996-12-20hrcl_ecf_N0002.fits

⁶ The National Radio Astronomy Observatory is a facility of the National Science Foundation operated under cooperative agreement by Associated Universities, Inc.

two EMSS clusters, MS1621 and MS2053, are published in Stocke et al. (1999). Radio maps from the Faint Images of the Radio Sky at 20cm (FIRST; Becker et al. 1995) are also available for MS1621. Eric Perlman kindly provided the 1.4 GHz radio maps and source identifications for two WARPS clusters (RXJ2302 and RXJ1415). The 1.4 GHz radio map of RXJ1053 was provided by Chris Carilli at NRAO. This observation was obtained in the spectral-line mode in the A-configuration under the VLA Program AC587 and it is the deepest radio image in our sample with a 3σ rms of 0.03 mJy. For the remaining clusters, RXJ0152 and RXJ0849, we utilized 1.4 GHz maps retrieved from the VLA archives. Higher resolution A-array maps for two clusters (MS1621 and RXJ0152) were reduced in a similar manner. For RXJ0152, a lower-resolution B-array map does not go deep enough for our purposes, but the A-array map does. Therefore, we use the A-array map to identify radio sources, but use the B-array map to measure a source flux, so there is less missing flux for the extended sources.

Table 3 lists the VLA 1.4 GHz radio observations for our $0.4 < z < 1.2$ cluster sample, including the VLA program ID and array configuration, the flux density limit, and the K-corrected radio power and luminosity limit for a source located at the cluster redshift. The flux density limit is the 3σ rms in mJy/Beam at the edge of our survey region (i.e., 1 Mpc from the cluster center). The radio power limits for our mid- z clusters are similar to our low- z cluster sample presented in Paper I ($P_{1.4\text{GHz}} \geq 3 \times 10^{23}$ W Hz $^{-1}$). However, for our high- z cluster sample, the radio power limits are slightly higher at $P_{1.4\text{GHz}} \geq 5 \times 10^{23}$ W Hz $^{-1}$, and thus we set the latter value as the radio power limit for our survey in this paper. RXJ0910 and RXJ0849 are excluded from the subsequent radio-related analyses, as the 1.4 GHz map 3σ rms falls 2–3 times above our selected radio limit. Also, the redshift limit of our cluster radio galaxies drops from $z=1.26$ to $z=1.13$ when we exclude RXJ0849. The X-ray observations of these two clusters are within our X-ray luminosity limits (refer to Column 8 of Table 2) and hence are included in later X-ray-related statistics. Thus, our radio galaxy sample extends to $z=1.1$, while our XPS sample extends to $z=1.2$.

3.3. Optical Imaging

The color-magnitude diagrams of clusters generally display a tight color sequence for the cluster ellipticals, i.e., the CRS. Two-color images of our cluster fields provide a simple classification scheme for cluster galaxies, particularly if the chosen filters span the Ca HK $\lambda 4000$ break at the cluster redshift to give the maximum contrast to the CRS. Table 4 lists the optical colors utilized for each $z > 0.4$ cluster, the observed mean color of CRS galaxies and the 3σ spread (with the analysis described in §4.1), the expected color of a passive elliptical, as estimated from Tables 6–8 in Fukugita et al. (1995), the 3σ limiting magnitude of the optical images, and the source of the survey images. The optical imaging data are summarized below.

Archival Hubble Space Telescope (*HST*) Advanced Camera for Surveys (ACS) images of four clusters in Table 4 (RXJ0152, RXJ1415, RXJ0910, and RXJ0849) were obtained from the Multimission Archive at Space

Telescope Science Institute (MAST). These clusters were observed with the F775W (Sloan i) and F850LP (Sloan z) filters, and RXJ0152 was also observed with the F625W (Sloan r) filter. The initial science goals from these imaging campaigns include the identification of the CRS in RXJ0849 (Program 9919, Mei et al. 2006b), the fraction of early-type galaxies in the cluster cores of RXJ0152 (Program 9290, Holden et al. 2006), and the detailed morphological classification of galaxies in RXJ0152, RXJ0910, and RXJ0849 (Postman et al. 2005). These two-color images, which cover the inner 1 Mpc radius from the cluster center, were reprocessed with Multidrizzle⁷ to correct image distortions, to identify and remove cosmic rays, and to combine dithered images from multiple visits. For the remaining 8 clusters listed in Table 4, *HST* archival imaging does not fully survey 1 Mpc from the cluster center, or the images do not survey down to the required limiting magnitude, and/or the imaging does not exist in the requisite filters for this study.

For RXJ1053, two-color optical images (Sloan i and z), obtained with Suprime-Cam on the Subaru 8.2m telescope at Mauna Kea, were provided by Yasuhiro Hashimoto. For MS1621, two-color optical images (Sloan i and z) were obtained from the Sloan Digital Sky Survey Data Release 6 (SDSS DR6; Adelman-McCarthy et al. 2008). In Spring 2006 we obtained Sloan (r, i) images of RXJ1221, RXJ1350, and RXJ1716 with SPICam on the Astrophysical Research Consortium (ARC) 3.5m Telescope at the Apache Point Observatory (APO). The FOV of SPICam is 4.8×4.8 arcmin, which adequately covers the entire 1 Mpc radius region for these three clusters at $0.7 < z < 0.8$. We used the Image Reduction and Analysis Facility (IRAF), v2.14.1, from the National Optical Astronomy Observatory (NOAO) in the usual manner to bias-subtract and flat-field individual images. Images were aligned and subsequently stacked with the IRAF task IMCOMBINE to produce one final image. United States Naval Observatory (USNO) B catalog stars (Monet et al. 2003) were used to correct the image astrometry. In-field SDSS stars were used to determine the photometric zero-points and color terms for images of RXJ1221 and RXJ1350, while off-field SDSS stars were used to calibrate RXJ1716. Using the tabulated values of $E(B-V)$ retrieved from the NASA/IPAC Extragalactic Database (NED) and based on the infrared dust maps of Schlegel et al. (1998), source magnitudes are corrected for the foreground Galactic extinction in each filter, by using the empirical relationships presented by Schneider et al. (2002). For these clusters, $E(B-V) \leq 0.08$.

For the APO, Subaru, and *HST* images, we used the Picture Processing Program (PPP; Yee 1991) to detect and classify objects as stars or galaxies. PPP is a robust detection algorithm, especially in crowded fields, such as galaxy clusters. Additionally, total source magnitudes are calculated using optimal extraction radii that are based on photometric growth curves. These PPP magnitudes have been shown to be highly accurate measurements (± 0.03 magnitudes, Yee et al. 1996) of total galaxy magnitudes down to the limiting magnitude of the image. For the *HST* images, the photometric zeropoints were obtained from the *HST* ACS website⁸. For the APO

⁷ <http://stdas.stsci.edu/multidrizzle/>

⁸ <http://www.stsci.edu/hst/acs/analysis/zeropoints>

and Subaru images, the photometric zeropoints and color terms were determined using SDSS DR6 objects in the image's FOV.

Two-color optical images (Sloan r and i) and photometry of MS2053, RXJ2302, and RXJ1113 were obtained from the Chandra Multiwavelength Project (ChAMP) (Green et al. 2004). ChAMP is a wide-area ($\sim 14 \text{ deg}^2$) serendipitous survey of 100 *Chandra* observations compiled to detect XPSs at $F_{0.3-8.0 \text{ keV}} \geq 10^{-14} - 10^{-15} \text{ erg cm}^{-2} \text{ s}^{-1}$ that are used to study the evolution of luminous AGN (e.g., Kim et al. 2004; Constantin et al. 2009; Haggard et al. 2010). Wide-field optical images of ChAMP clusters were obtained with the Mosaic CCD cameras (Muller et al. 1998) on the NOAO 4-meter telescopes. Details of the image reductions and photometry with SExtractor (Bertin & Arnouts 1996) can be found in Green et al. (2004).

4. OBSERVATIONAL RESULTS

4.1. Cluster Red Sequence and Composite Color-Magnitude Diagrams

The most massive, and hence most luminous, early-type cluster galaxies probably formed at $z > 2.0$ (e.g., Stanford et al. 1998; Blakeslee et al. 2006). With similar colors down to $M^* + 3$ (Ellis et al. 1997), these objects form a CRS in color-magnitude diagrams. Several optically-selected cluster surveys (e.g., Red-sequence Cluster Survey (RCS), Gladders & Yee 2005; MaxBCG method, Koester et al. 2007) utilize this ubiquitous feature to photometrically identify clusters in optical surveys. Color comparisons between objects with or without CRS colors provide simple galaxy classifications, i.e., objects bluer than CRS galaxies could be late-type cluster galaxies or foreground objects along the line-of-sight. Objects with redder colors than CRS galaxies could be background objects or highly-reddened cluster galaxies.

In Paper I, we examined radio galaxies and XPSs in $M_r < -20.8$ galaxies ($\approx L^*$ galaxies). Here, we assume pure luminosity evolution (PLE) of the CRS galaxies to limit our study to AGN hosts with $M_r \leq -21.2$ for $0.4 < z < 0.8$ clusters or $M_r \leq -21.6$ for $0.8 < z < 1.2$ clusters. These magnitude limits correspond approximately to L^* once the PLE corrections of $\Delta 0.1$ magnitudes per $\Delta 0.1$ redshift (van Dokkum & van der Marel 2007) are applied. Foreground and background galaxies are statistically subtracted from each cluster by using the Sloan r -band background counts from Yasuda et al. (2001) for clusters with a limiting $m_r < 21.0$ or using the COSMOS i -band background counts from Capak et al. (2007) with a limiting $m_i < 26.0$. We determine the mean CRS color by fitting a bimodal Gaussian distribution to both the red and blue galaxy populations as a function of color (similar to Paper I). After identifying galaxies within 3σ of the mean CRS color, we define the CRS more precisely by fitting a line to the observed color versus magnitude of these sources and thus verifying the well-known “tilt” of the CRS in cluster color-magnitude diagrams (e.g., Visvanathan & Sandage 1977).

For the four highest redshift clusters in our sample (RXJ1415, RXJ0910, RXJ1053, and RXJ0848) no statistical subtraction of background galaxies was applied because the estimated number of background objects in a given magnitude bin in a small region of sky ex-

ceeds the observed galaxy counts in our optical images. In a weak-lensing study of RXJ0849, Jee et al. (2006) found no significant excess in the background galaxy counts due to cluster galaxies at $24.0 < m_z < 27.0$. Similarly, Mei et al. (2006a) estimated that the background contamination is small for early-type galaxies (i.e., CRS galaxies) in RXJ0910. Additionally, the optical magnitudes of the BCGs in RXJ0910 and RXJ0849 are $i = 22.9$ and $i = 23.5$, respectively, and potential CRS galaxies are expected to be fainter than this magnitude. The CRS colors of RXJ0910 and RXJ0849 are ≈ 0.5 magnitudes redder than the typical SDSS field galaxies, which have $(i-z)$ colors between 0.0 and 0.5 (Newberg et al. 1999). In the four highest redshift clusters listed above we assume that any galaxy with CRS colors is a likely cluster member. Therefore, we fit a single Gaussian component to the expected CRS galaxy population in the color-magnitude diagrams of these four clusters to determine the mean color of typical CRS galaxies.

For our $0.4 < z < 1.0$ clusters, we do not expect over-subtraction of background galaxies to be a potential problem because of the field-to-field differences in the background galaxy counts due to cosmic variance. In their study of the global environments around bright quasars, Yee et al. (1986) estimated the uncertainty in the background galaxy counts using several control fields and find it to be 1.3 times larger than Poisson errors alone. These authors attribute the increased variance to intrinsic clustering of galaxies. Therefore, we expect the error on the cumulative CRS galaxy number for our $0.4 < z < 1.0$ clusters to be larger than pure counting statistics alone. For simplicity we assume Poisson errors on our estimates of CRS galaxy counts.

Figures 2–4 display the composite color-magnitude diagrams of our low- z , mid- z , and high- z cluster samples, respectively, as a function of the object's rest-frame magnitude at the cluster redshift. Rest-frame magnitudes are calculated using the k -corrections for E0 galaxies from Fukugita et al. (1995). These k -corrections slightly overestimate the rest-frame magnitudes of bluer cluster galaxies. The “color difference” in Figures 2–4 is the magnitude difference between the object's observed color and the mean CRS color at the given rest-frame magnitude (Columns 3–4 of Table 4).

The color difference is $(g-r)$ in Figure 2, with the exception of MS2137, A1995, MS1358, and A370 where the color difference is $(r-i)$. In Figure 3 the color difference is $(r-i)$, while in Figure 4 it is $(i-z)$ with the exception of RXJ1350 and RXJ1716 where the color difference is $(r-i)$. All optical sources within a 1 Mpc projected radius of the cluster center are displayed (small black dots in Figures 2–4). Optical sources that are 2–4 magnitudes brighter than the BCGs are most likely foreground objects. The host galaxies of radio galaxies and XPSs, described in the next section, at $L \geq L^*$ and corrected for PLE are also identified in Figures 2–4 (radio sources in red; XPSs in blue). Figure 2 is a modification of Figure 2 in Paper I, in that we have overlaid the host galaxies of the non-cluster radio galaxies and XPSs for comparison. The vertical dashed-line identifies L^* galaxies in the specified filter, corrected for PLE for the mean of that redshift range. The short-dashed horizontal lines bound the maximum spread of 0.33 magnitudes from the mean CRS color (see Column 3 of Table 4).

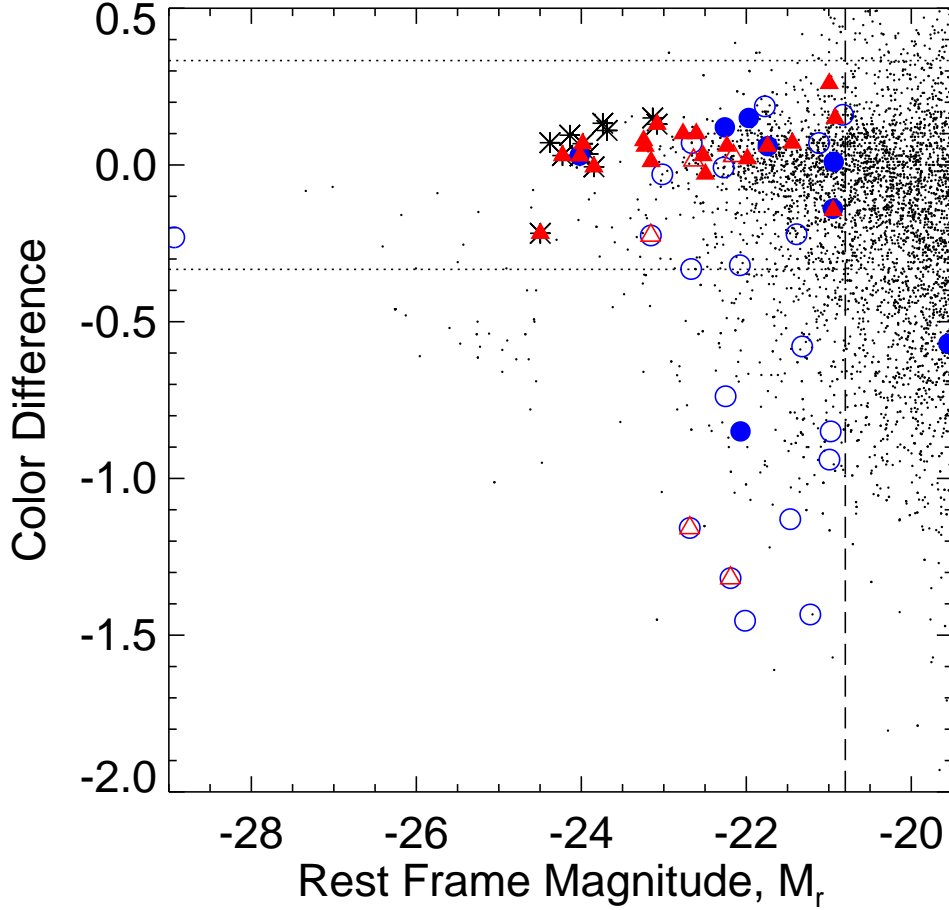


FIG. 2.— Composite color-magnitude diagram for eleven $0.2 < z < 0.4$ clusters. The color difference is the magnitude difference between the object's observed ($g-r$) color and the mean CRS ($g-r$) color of the cluster, with the exception of MS2137, A1995, MS1358, and A370 for which the color difference is $(r-i)$. Small black dots are optical sources located within a 1 Mpc projected radius of the cluster X-ray emission centroid. Filled red triangles (blue circles) are host galaxies of cluster radio galaxies (XPSs). Open red triangles (blue circles) are host galaxies of non-cluster radio sources (XPSs). Brightest cluster galaxies are identified with an asterisk. The horizontal short-dashed lines mark ± 0.33 mags from the mean CRS color of each cluster, which is the maximum width of the CRS population in these clusters (see Table 4). The vertical long-dashed line marks L^* galaxies with $M_r^* \approx -20.8$. All AGN at $L \geq L^*$ have been spectroscopically confirmed. This is a modified version of Figure 2 in Paper I.

4.2. Radio Galaxies and XPS Detections

For our $z > 0.4$ clusters, Table 5 lists radio sources with flux densities which correspond to $P_{1.4\text{GHz}} \geq 5 \times 10^{23} \text{ W Hz}^{-1}$ at the cluster redshift. (Table 3 in Paper I lists the radio sources for the $0.2 < z < 0.4$ clusters.) Table 5 lists the number identifier used in subsequent plots, the RA/DEC of the radio source, the redshift if known, the optical magnitude and color of the host galaxy, the mean CRS color for the cluster, and the projected distance, or “radius”, from the cluster X-ray emission centroid (listed in Columns 2-3 of Table 2). Column 12 lists the observed 1.4 GHz flux density in mJy. If the source redshift is known, then Column 13 lists the 1.4 GHz radio power assuming that $F_\nu \propto \nu^{-\alpha}$ with a spectral index, $\alpha = 0.7$. For sources with unknown redshifts, Column 13 lists

the radio power of the source if located at the cluster redshift (identified in parentheses). Assuming a power-law spectrum with $\Gamma = 1.7$ ($N_E \propto E^{-\Gamma}$), Columns 14-15 of Table 5 lists the observed X-ray flux and luminosity for the radio source if at z_{cluster} , or a limit on those values for an X-ray non-detection. The X-ray flux limits are estimated as 3σ above the background at the source position.

Of the 26 detected radio sources in the $z > 0.4$ cluster sample, 24 radio sources have $L \geq L^*$ optical counterparts if at z_{cluster} . Eleven are spectroscopically-confirmed cluster members, all with CRS colors, and 3 are spectroscopically-confirmed non-cluster members all with non-CRS colors. The remaining 10 radio sources (8 with CRS colors, including Source 10 in Table 5, and 2

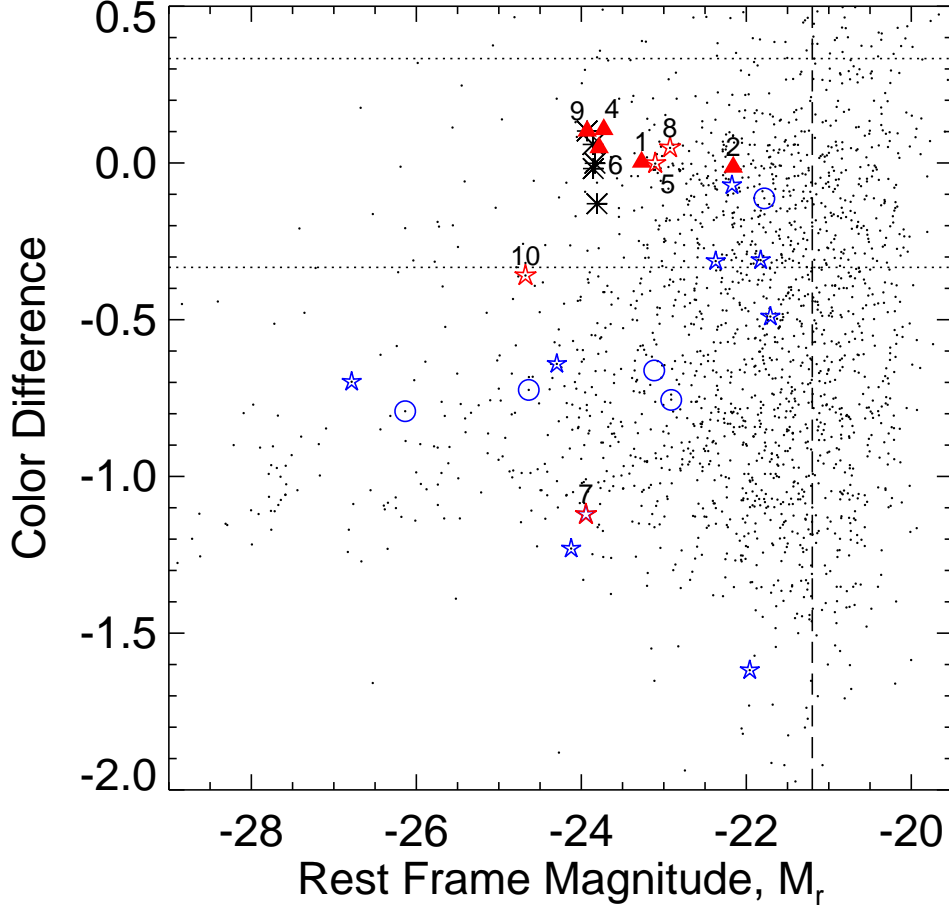


FIG. 3.— Composite color-magnitude diagram for five $0.4 < z < 0.8$ clusters. The “color difference” is the magnitude difference between the object’s observed ($r-i$) color and the mean CRS ($r-i$) color of the cluster as listed in Table 4. Symbols and dashed lines are similar to Figure 2. Open red (blue) stars are the host galaxies of radio galaxies (XPSs) with unknown redshifts. The vertical long-dashed line marks $M_r^* \approx -21.2$ at $z=0.6$, corrected for 0.4 magnitudes of pure luminosity evolution (see §4.1 for details). Host galaxies of the radio sources with unknown redshifts and located on or near the CRS (i.e., between the short-dashed horizontal lines) are assumed to be cluster members (see §6 for details). Number identifiers correspond to the radio sources listed in Table 5.

with non-CRS color) have unknown redshifts. Thus, the sample of radio sources listed in Table 5 is 54% spectroscopically complete in total and 58% complete for radio sources with CRS host galaxies.

In Figures 3–4, these radio sources are identified by red closed (open) triangles for cluster (non-cluster) sources and by red open stars for radio sources with unknown redshifts. These radio sources are labeled with the number identifiers listed in Column 1 of Table 5, excepting MS1621-R3 and RXJ1716-R3 with optical non-detections at m_{lim} in the optical images. Based on the radio source redshift or host galaxy color, Column 3 of Table 5 lists a code for our best estimate of a radio source’s association with the cluster. (See tablenote (3) of Table 5 for details.) Five of the radio sources listed in Table 5 have X-ray counterparts above the required

X-ray luminosity limit at the cluster redshift.

For our $z > 0.4$ clusters Table 6 only lists XPSs that are spectroscopically-confirmed cluster members, while Table 11 in the Appendix lists our entire sample of XPSs at $L_{0.3-8.0\text{keV}} \geq 5 \times 10^{42} \text{ erg s}^{-1}$ if located at the cluster redshift. These two tables include the source number (including the letter identifiers used in subsequent plots in parentheses), the RA/DEC of the XPS, the source redshift if known, the observed net broadband (0.3–8.0 keV) counts and resulting X-ray flux and luminosity. The X-ray luminosity at the cluster redshift is tabulated for XPSs with unknown redshifts. Also listed is the projected distance of the XPS from the cluster center in Mpc (“radius” in Table 11), the host galaxy’s optical magnitude and color, and the 1.4 GHz radio power or power limit for each XPS.

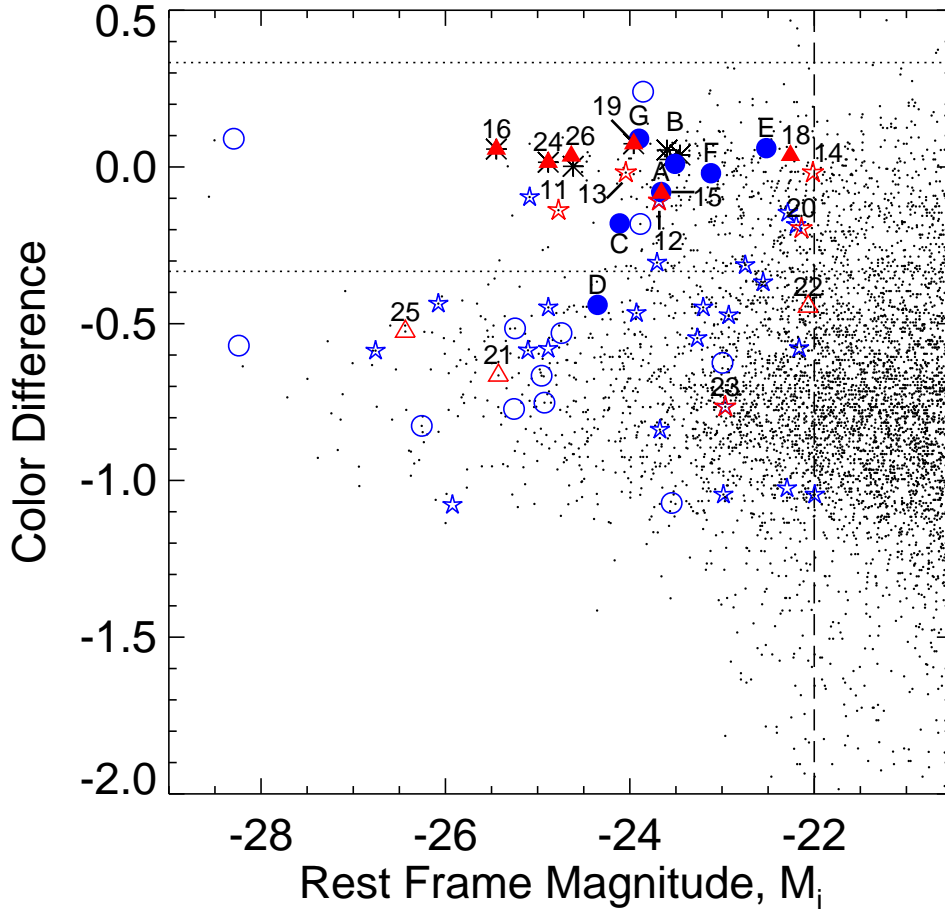


FIG. 4.— Composite color-magnitude diagram for seven $0.8 < z < 1.2$ clusters. The “color difference” is the magnitude difference between the object’s observed ($i-z$) color and the mean CRS ($i-z$) color of the cluster, as listed in Table 4, with the exception of RXJ1350 and RXJ1716 for which the color difference is $(r-i)$. Symbols and horizontal dashed lines are similar to Figure 3. The vertical long-dashed line marks $M_i^* \approx -22.0$ at $z=1.0$, corrected for 0.8 magnitudes of pure luminosity evolution. Number identifiers correspond to the radio sources listed in Table 5, while letter identifiers correspond to the seven XPSs listed in Column 1 of Table 6.

Of the 86 detected XPSs listed in Table 11, 67 XPSs have optical counterparts on our images. However, our working sample consists of only 56 XPSs at $L_{0.3-8.0\text{keV}} \geq 5 \times 10^{42} \text{ erg s}^{-1}$ and hosted by $L \geq L^*$ galaxies if at z_{cluster} . The redshifts for some XPSs come from the literature, which includes the optical follow-up campaigns of ChaMP and the Serendipitous Extragalactic X-ray Source Identification (SEXSI, Eckart et al. 2006). The SEXSI survey is a 2 deg^2 survey of hard X-ray-selected AGN that complements the *Chandra* Deep Fields to detect XPSs with fluxes between 10^{-13} – $10^{-15} \text{ erg cm}^{-2} \text{ s}^{-1}$.

In Figures 3–4, XPSs are identified by blue closed (open) circles for cluster (non-cluster) sources and by blue open stars for the XPSs with unknown redshifts. Our working sample of the XPSs listed in Table 11 is 45% spectroscopically complete, which increases to 55%

for a subset of XPSs with CRS host galaxies only. The cluster XPS population is considerably less well-defined than the cluster radio galaxy population in our sample due to lack of redshifts. Column 3 of Table 11 lists a classification tag for the XPSs based on spectroscopy and/or host galaxy color relative to the CRS (see tablenote (3) of Table 11 for more details).

5. RADIO GALAXIES IN $0.4 < z < 1.1$ CLUSTERS

5.1. Statistical Sample

In Paper I, we detected 26 radio galaxies at $P_{1.4\text{GHz}} \geq 3 \times 10^{23} \text{ W Hz}^{-1}$ hosted by $L \geq L^*$ galaxies located within 1 Mpc of the cluster core. We found that 87% of the CRS radio galaxies are cluster members, whereas, none of the bluer radio galaxies are cluster members. This result is consistent with the expectation that at low- z radio-loud objects are hosted by early-type

galaxies (Ledlow & Owen 1995). Thus, we can assume that nearly all high- z radio galaxies with CRS colors are cluster members. Also, 17 of 20 cluster radio galaxies from Paper I are detected at $P_{1.4\text{GHz}} \geq 5 \times 10^{23} \text{ W Hz}^{-1}$ (the radio limit in this present work). The most luminous radio source at low- z (RXJ1758-R6 in Table 3 from Paper I) is detected at $P_{1.4\text{GHz}} = 8.1 \times 10^{24} \text{ W Hz}^{-1}$, just below the nominal FR I/FR II power-level boundary ($P_{1.4\text{GHz}} \sim 10^{25} \text{ W Hz}^{-1}$; Ledlow & Owen 1996).

For the ten $0.4 < z < 1.1$ clusters (excluding RXJ0910 and RXJ0849) Table 5 lists the 26 radio sources detected with flux densities sufficient to have $P_{1.4\text{GHz}} \geq 5 \times 10^{23} \text{ W Hz}^{-1}$ at the cluster redshift. Setting aside the 14 sources with spectroscopic redshifts (11 are spectroscopically-confirmed cluster members with CRS colors), of the remaining 12 radio sources, 8 have CRS colors, 2 non-CRS colors, and 2 have no optical counterparts. While all 8 radio sources with CRS colors should be considered likely cluster members, if we extrapolate our low- z results, we conservatively identify only 6 as highly-likely cluster members for a total of 17 (of 19 or 87%) cluster radio galaxies in our $0.4 < z < 1.1$ sample.

Because there are no obviously distinguishing photometric differences between the 8 CRS radio galaxies lacking spectroscopy, we have chosen two specific sources as non-cluster members as follows: (1) we discard the lowest flux source as non-cluster (RXJ1350-R4, Source 14 in Table 5); (2) we discard Source 10 (RX J1113-R1) in Table 5 due to its unusual nature as follows. Source 10 is located near the edge of the CRS in Figure 3. This source is both 0.6 magnitudes brighter and 0.3 magnitudes bluer than the other BCGs in the mid- z redshift range. At the cluster redshift of $z = 0.72$, the [O II] $\lambda 3727$ emission line would fall in the Sloan r filter and [O III] $\lambda 5007$ would fall just redward of the Sloan i filter. If the flux contribution from [O II] $\lambda 3727$ is $\sim 25\%$ of the total light in this filter, Source 10 would appear bluer than the CRS at the cluster redshift, similar to the BCG in MS 1455.0+2232 at $z = 0.25$ presented in Paper I. However, this source is not located at the cluster center, but rather at a projected distance of 500 kpc from the core. Source 10 is also one magnitude brighter than the galaxy identified as the RXJ1113 BCG due to its coincidence with the X-ray centroid.

For the above reasons, Source 10 is a good candidate for being a foreground source. Therefore, we assign Sources 14 and 10 as non-cluster radio sources. The exclusion of these two sources does not alter the statistical difference between the low- z and high- z radio luminosity functions presented in §6. Likewise, there is no strong evidence for “blue” radio galaxies in this sample, and there were none at low- z . We assign the 2 high- z blue radio sources without redshifts as highly-unlikely cluster members. In summary, we conservatively identify 17 radio galaxies in Table 5, all on the CRS, as our high- z radio-loud cluster sample. However, future spectroscopy is required to verify this assessment and to search for blue radio galaxies in high- z clusters.

Figure 5 displays the distribution of the cluster radio galaxy powers with (open, hatched, shaded) regions corresponding to (low- z , mid- z , high- z) radio galaxies, respectively. The right panel of Figure 5 displays the radio-loud BCGs only (6 at low- z , 2 at mid- z , 3 at

high- z). The average radio power of cluster radio galaxies is $(2.2 \pm 1.7, 14.5 \pm 13.9, 78.8 \pm 232.0) \times 10^{24} \text{ W Hz}^{-1}$ in the (low- z , mid- z , high- z) redshift bins, respectively. Even if we exclude RXJ1716-R1 ($z = 0.8$), the FR II source at $P_{1.4\text{GHz}} = 7.7 \times 10^{26} \text{ W Hz}^{-1}$ (see §5.3), the average radio power of $0.4 < z < 1.1$ cluster radio galaxies is $9.4 \pm 10.9 \times 10^{24} \text{ W Hz}^{-1}$. The spread in the average radio powers for $z > 0.4$ cluster radio galaxies suggest that some are more luminous than their low- z counterparts presented in Paper I. For BCG radio sources alone, at low- z the average radio power is $1.9 \pm 1.1 \times 10^{24} \text{ W Hz}^{-1}$, while at $0.4 < z < 1.1$ it is $1.8 \pm 1.3 \times 10^{25} \text{ W Hz}^{-1}$, evidence that BCG radio sources have faded by about an order of magnitude from $0.4 < z < 1.1$ to $0.2 < z < 0.4$. This is consistent with earlier results from samples that were selected differently (e.g., Harvanek et al. 2001).

5.2. Radial Distribution

Figure 6 displays the cumulative radial distribution of (20, 7, 10) cluster radio galaxies in the (low- z , mid- z , high- z) cluster samples as a function of the projected radius from the cluster center (shown as a dotted red line) compared to the cumulative radial distribution of CRS galaxies (black dot-dashed line). In Paper I, we used a two-sided Kolmogorov-Smirnov (K-S) test to determine the probability that the cumulative distribution of two samples are drawn from the same parent population (Press et al. 1992). We concluded that the radial distributions of the low- z cluster radio galaxy population and the CRS galaxy population as a whole are inconsistent with being drawn from the same parent population and that the radio galaxies are more centrally concentrated than the CRS galaxies at the 5.7σ level (see left panel of Figure 6).

Table 7 summarizes the K-S test results between the cumulative radial distributions of the radio galaxies in our low- z , mid- z , and high- z samples compared to their respective CRS galaxy population. In Table 7 we include the value of the K-S D-statistic, the probability that the two samples are drawn from the same parent population, and the statistical significance of this probability. As seen in the middle panel of Figure 6, the mid- z cluster radio galaxy population appears to remain centrally concentrated compared to CRS galaxies at the 5.9σ level and consistent with the results at low- z . However, the radial distribution of the radio galaxies in the $0.8 < z < 1.1$ clusters (right panel) approximately tracks that of the CRS galaxies.

The probability of a cluster galaxy hosting a radio source increases with optical magnitude (Ledlow & Owen 1996) and the BCG, as the most massive cluster galaxy, is more likely to host a radio source than other cluster galaxies (Best et al. 2007). Is the special location of the radio-loud BCG at the cluster center skewing the analysis and only making the population appear more centrally concentrated compared to the CRS galaxies? To test this, we remove the BCGs from the radial distribution analysis above. The cumulative radial distribution of this reduced sample (solid green line in Figure 6) remains statistically different from the underlying CRS galaxy population at the $(4.7\sigma, 4.2\sigma, 4.0\sigma)$ level for the (low- z , mid- z , high- z) cluster sample. From Figure 6, the cumulative fraction

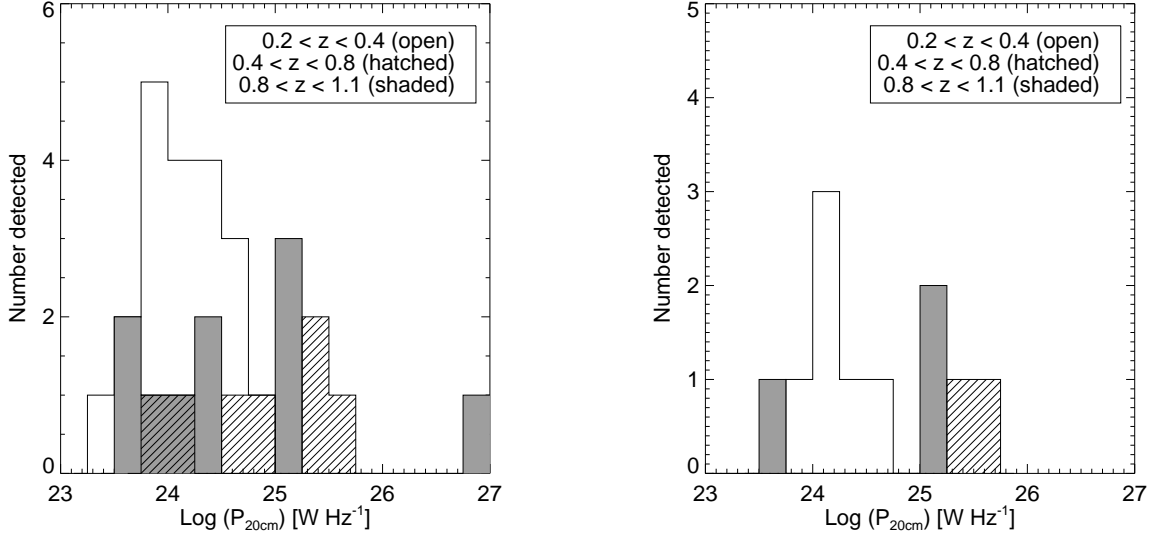


FIG. 5.— Histogram of radio galaxy powers in 21 clusters at $0.2 < z < 1.1$ (left panel) and of cluster BCGs only (right panel). The open histogram displays the number of radio sources with $\log(P_{1.4GHz}) \geq 23.5$ W Hz^{-1} at $0.2 < z < 0.4$ ($N=20$), while the hatched histogram displays the number of sources at $0.4 < z < 0.8$ with $\log(P_{1.4GHz}) > 23.5$ ($N=8$). The shaded histogram displays the number of radio sources at $0.8 < z < 1.1$ with $\log(P_{1.4GHz}) > 23.7$ W Hz^{-1} ($N=11$). The right panel shows that the decline in radio power with redshift is more dramatic for the BCGs in this cluster sample.

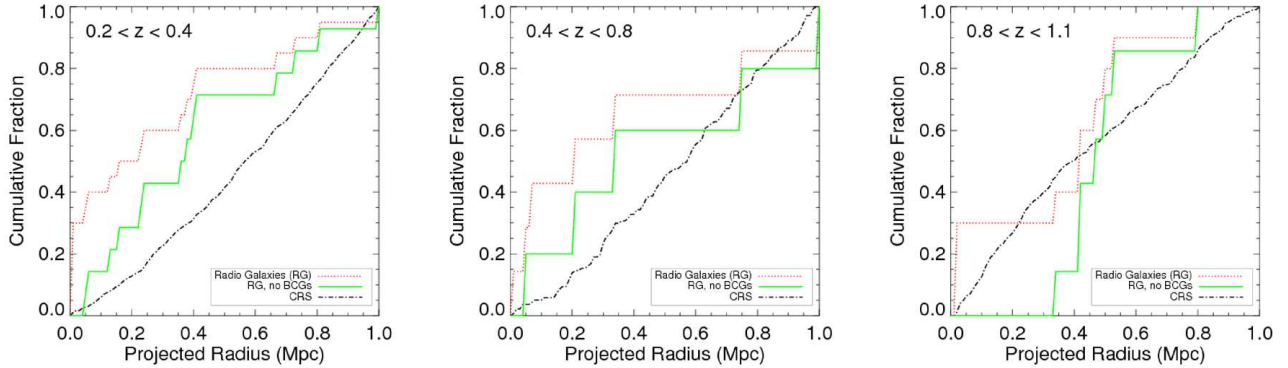


FIG. 6.— Cumulative radial distributions of cluster radio galaxies relative to CRS galaxies in three redshift bins. In each panel, the cumulative fraction of cluster radio galaxies (dotted red line), as a function of projected distance from the cluster X-ray emission centroid, is compared to the CRS galaxy (black dot-dashed line) distribution. Also displayed is the cumulative fraction of cluster radio galaxies excluding the radio-loud BCGs (solid green line). Notice that the cluster radio galaxy population at $0.2 < z < 0.8$ (left and middle panels) appears more centrally concentrated than the CRS galaxies, while at $z > 0.8$ (rightmost panel), there appears to be an absence of radio-loud galaxies near the cluster centers. However, the overall impression is that radio galaxies become more centrally concentrated with cosmic time (see §5.2 and Table 7 for statistics).

of radio galaxies within 500 kpc of the cluster core is $(72 \pm 23\%, 60 \pm 35\%, 57 \pm 29\%)$ in the (low- z , mid- z , and high- z) sample. Moreover, this fraction decreases to $(43 \pm 17\%, 40 \pm 28\%, 0 \pm 14\%)$ within 300 kpc of the cluster center. Although the data are insufficient to produce a significant result, we note that our higher redshift clusters have few AGN (apart from the BCG) in the cluster cores, suggesting that radio sources in clusters become more centrally-concentrated over cosmic time.

5.3. An FR II Source in a $z=0.8$ Cluster

The identification of FR II radio sources in the high- z cluster sample is somewhat unexpected given that none were found in the low- z cluster sample from Paper I. However, it has been known for some time that some luminous quasars and FR II radio galaxies are found in clusters at $z \geq 0.5$ (e.g., Ellingson et al. 1991; Hill & Lilly 1991; Harvanek et al. 2001). Those detections suggest that FR IIs located in rich clusters at high redshift rapidly evolve in luminosity to become FR Is at $z=0$. Because the fading of cluster FR IIs occurs over a similar time-frame (~ 1 Gyr) as the development of a deep gravitational potential well and a hotter ICM in clusters,

these results suggest that the AGN evolution is linked to the evolution of the cluster environment (Harvanek et al. 2001). Therefore, a detection of an FR II in our sample at $z \approx 0.8$ is evidence supporting this idea.

A contour map of the VLA 1.4 GHz continuum image of RXJ1716 ($z = 0.809$) is displayed in Figure 7 with the crosses marking the optical counterpart closest to the radio position. As noted in §3.2, RXJ1716 was observed for 2 hours with the VLA at 1.4 GHz in its standard B-configuration (VLA program AS873). Four radio sources, listed in Table 5, are detected above the 3σ map rms of 0.21 mJy/beam. The BCG, source RXJ1716-R2 in Table 5, is located at the center of Figure 7. However, RXJ1716-R1, which is located $1.2'$ west of the BCG (or at a projected radius of 530 kpc), has a clear double-lobed radio morphology (angular extent of $\sim 18''$ or 135 kpc) and a much higher radio power ($P_{1.4\text{GHz}} = 7.7 \times 10^{26}$ W Hz $^{-1}$). These properties clearly identify it as an FR II radio galaxy.

RXJ1716-R1 is also detected at 4.85 GHz and 365 MHz (see White & Becker 1992), 74 MHz (Cooray et al. 1998) and 28.5 GHz (Cohen et al. 2007). Even in the NRAO VLA Sky Survey (NVSS), RXJ1716-R1 appears extended, as noted by Cooray et al. (1998), although the lower angular resolution of the D-configuration does not clearly show the double-lobed structure (see Figure 4 in Cooray et al. 1998) that is resolved in Figure 7. Based on multi-frequency radio observations, the spectral index, α , is 1.1 between 6cm and 20cm, and 1.0 between 80cm and 20cm (White & Becker 1992). This steep spectral index suggests that the electron population in this source is older than in typical FR II radio galaxies. A higher resolution map might be expected to show the “fat double” morphology seen in steep-spectrum FR IIs in clusters (Harvanek & Stocke 2002).

RXJ1716-R1 is also detected as a *Chandra* XPS with $L_{0.3-8.0\text{keV}} = 46.5 \pm 6.6 \times 10^{42}$ erg s $^{-1}$. The host galaxy ($i = 21.23$) appears elliptical in our ARC 3.5m optical images (FWHM $\approx 1.3''$), as well as in HST WFPC images (Proposal ID 7293). SEXSI identified RXJ1716-R1 (SEXSI J171636.9+670829; Harrison et al. 2003) as an emission-line galaxy (Eckart et al. 2006) at $z = 0.795$. Emission lines of [O II] and [O III], along with a strong Ca HK break are detected (private communication, Megan Eckart). The radial velocity of this source is 0.9σ from the cluster centroid velocity, where σ is the observed cluster velocity dispersion of 1522 km s $^{-1}$ (Gioia et al. 1999), and so consistent with being a cluster member and not an in-falling galaxy seen projected onto the cluster center. Unlike the radio-loud galaxies situated in nearby clusters found in Paper I, RXJ1716-R1 is located 530 kpc from the cluster core, in a region of lower ICM density. The *Chandra* image does not reveal any noticeable “cavities” in the X-ray emitting ICM at the location of the radio lobes, although the X-ray surface brightness is quite low at that large radial distance.

6. THE RADIO LUMINOSITY FUNCTION OF CLUSTER RADIO GALAXIES IN COMA CLUSTER PROGENITORS

Using the statistical sample of the 17 cluster radio galaxies from the previous section, we determine the radio active fraction (RAF) of cluster CRS galaxies and

construct the radio luminosity function (RLF) of radio galaxies in our cluster sample between $0.2 < z < 1.1$. In eleven low- z clusters we identified 665 $L \geq L^*$ CRS galaxies and also 17 cluster radio galaxies at $P_{1.4\text{GHz}} \geq 5 \times 10^{23}$ W Hz $^{-1}$ within 1 Mpc of the cluster core (see Paper I), yielding 1.5 ± 0.5 radio galaxies *per cluster* or a cluster RAF for CRS galaxies of $2.5 \pm 0.8\%$ (Poisson statistics; Gehrels 1986). Due to the small number of radio sources in the mid- z and high- z bins (7 and 10 sources, respectively), we combine them together into the “combined high- z sample”. In ten $0.4 < z < 1.2$ clusters (not including RXJ0910 nor RXJ0849), we identified 443 $L \geq L^*$ CRS galaxies and 17 cluster radio galaxies, yielding 1.7 ± 0.5 radio galaxies *per cluster* or a cluster RAF of $3.8 \pm 1.2\%$ (Poisson statistics; Gehrels 1986). The cumulative binomial probability of detecting ≥ 17 radio galaxies in 443 CRS galaxies in our combined high- z sample based on the low- z results from Paper I is 6.6% and is therefore only marginal evidence for density evolution of the radio galaxy population in Coma Cluster progenitors between $0.2 < z < 1.1$.

As noted in §5.1, the spread in the average 1.4 GHz radio power of the $0.4 < z < 1.1$ cluster radio galaxies is larger than that at low- z . We quantify this luminosity evolution more precisely by constructing a univariate RLF. Table 8 lists the radio power bins used to construct the low- z and combined high- z RLF of radio galaxies in this cluster sample, including upper limits on the bins without radio detections. The highest radio power bin at $\log(P_{1.4\text{GHz}}) = 27.0$ W Hz $^{-1}$ includes only RXJ1716-R1, the cluster FR II at $\log(P_{1.4\text{GHz}}) = 26.8$ W Hz $^{-1}$ described in §5.3. Figure 8 is a log-log plot of the RAF fraction with respect to the CRS galaxies versus $\log(P_{1.4\text{GHz}})$.

6.1. Comparison With Previous Low- z Cluster Results

At FR I power levels between $23.6 < \log(P_{1.4\text{GHz}}) < 25.0$ W Hz $^{-1}$, we detect 17 cluster radio galaxies in 665 low- z CRS galaxies. (We adopt a working limit of 10^{25} W Hz $^{-1}$ for FR Is based upon the survey of Ledlow & Owen (1996) who find few FR Is above that power level and more FR IIs above 10^{26} W Hz $^{-1}$.) Given these statistics, we expect to detect 11 radio galaxies in 443 CRS galaxies at $0.4 < z < 1.1$ and we detect 10 sources consistent with the expectation. This result suggests little density or luminosity evolution in our $0.2 < z < 1.1$ radio galaxy population at FR I radio powers. However, we detect a substantial increase in the number of cluster radio galaxies at $25.0 < \log(P_{1.4\text{GHz}}) < 27.0$ W Hz $^{-1}$. At FR II radio power levels we detect 7 radio sources in our combined high- z cluster sample (of which 4 are located in the BCG), and none were detected at low- z in Paper I. Using the 7 detections in our combined high- z clusters to define a detection probability, we expect to detect 10.5 FR II power-level radio sources in 665 CRS galaxies at low- z and we detected none. The cumulative binomial probability of detecting no radio galaxies at low- z is 0.003% (3.3σ using binomial statistics). In Monte Carlo simulations consisting of 100,000 realization of our total low- z CRS sample, we find that there is only a 1.1% probability that our results would occur randomly (Gaussian significance of 2.6σ). Therefore, the radio galaxy population in our cluster samples differs at $\log(P_{1.4\text{GHz}}) > 25.0$

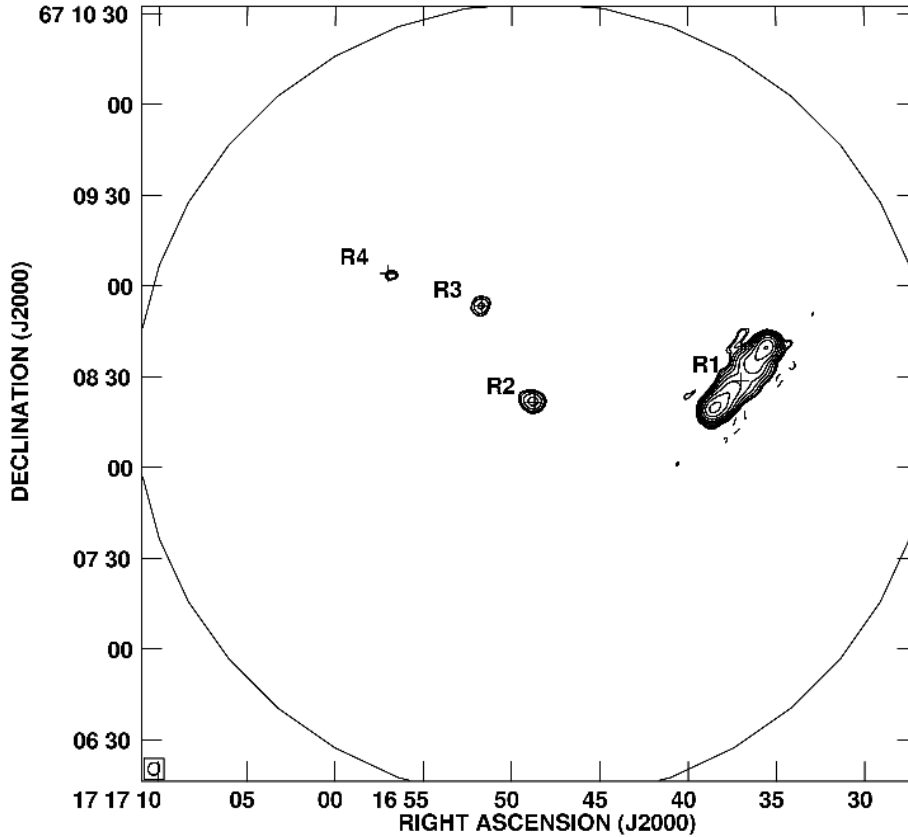


FIG. 7.— VLA 1.4 GHz radio contour map of RX J1716.6+6708. Of the four radio sources detected above the 3σ map rms of 0.21 mJy/Beam, R1, R2, and R4 are confirmed cluster members ($z_{\text{cluster}}=0.809$), while R3 is a confirmed non-cluster source (see Table 5 for source details). R2, near the map center, is located in the cluster BCG. However, R1, the double-lobed, FR II radio source, is located $1.2'$ West of the cluster center (≈ 530 kpc). The large outer circle marks a 1 Mpc projected radius from the cluster center, while the crosses mark the optical counterpart closest to the radio position. The continuum peak flux of the map is 7.1 mJy/Beam with contour levels of $0.42 \text{ mJy} \times (-1, 1, 1.18, 2, 4, 8, 16, 32, 64, 128, 256)$.

W Hz^{-1} . Unlike other high- z cluster radio galaxy surveys (e.g., Stocke et al. 1999; Branchesi et al. 2006), this evidence for the evolution of the RLF is more robust because it is entirely internal to our sample, avoids biases created by different selection and analysis methods, and uses a better sample selection technique. Table 9 (rows 1 and 6) summarizes the comparisons between the expected and detected number of radio galaxies in our low- z and combined high- z cluster samples.

Is this observed excess in the radio galaxy numbers at higher radio powers a result of our sample selection? To answer this question, we first compare our cluster RLFs to that of local Abell clusters at $z < 0.09$ from Ledlow & Owen (1996). Using 188 cluster radio galaxies, these authors computed the univariate and bivariate RLF of radio sources hosted by elliptical and S0 galaxies with $M_R < -20.5$ and $\log(P_{1.4\text{GHz}}) > 22 \text{ W Hz}^{-1}$ and located within 0.3 Abell radius (≈ 600 kpc) of the cluster center. Using Figure 3 from Paper I or Figure 6 in this work, we find that 60% of our CRS galaxies are located within 600 kpc of the cluster centers. Therefore, we apply this correction factor to be consistent with the Ledlow & Owen (1996) sample definition and exclude 2 radio galaxies from our low- z cluster sample (MS1455-R1 and MS1008-R1) and 3 radio galaxies from our $0.4 < z < 1.1$ cluster sample (MS1621-R4, RXJ1221-

R4, and RXJ1350-R1) that are outside that region.

Figure 9 displays the RLF of radio galaxies in Abell clusters from the Ledlow & Owen (1996) sample compared to the RLF of our eleven low- z clusters from Paper I (left panel) and our ten combined high- z clusters from this work (right panel). We adjust the Abell RLF by $+0.08$ in $\log(P_{1.4\text{GHz}})$ to account for the different cosmology assumed in their paper. At $23.6 < \log(P_{1.4\text{GHz}}) < 25.0 \text{ W Hz}^{-1}$, the RLFs of our low- z and combined high- z radio galaxies are consistent with the RLF measured by Ledlow & Owen (1996) (cumulative binomial probabilities of 66% and 85%, respectively). However, the RLF of radio galaxies in our combined high- z sample deviates noticeably at $\log(P_{1.4\text{GHz}}) > 25.0 \text{ W Hz}^{-1}$. At $z > 0.4$ we expect to detect 2.2 radio galaxies at $\log(P_{1.4\text{GHz}}) \geq 25.0 \text{ W Hz}^{-1}$, but we detect 6 radio galaxies above this power level, 5 of which are spectroscopically-confirmed cluster members. The cumulative binomial probability of detecting ≥ 6 radio sources at $\log(P_{1.4\text{GHz}}) > 25.0 \text{ W Hz}^{-1}$ in ten $0.4 < z < 1.1$ clusters is 2% and thus inconsistent with the expectation. Therefore, we conclude that the RLF for cluster radio galaxies does not significantly evolve from $0.2 < z < 0.4$ to the present epoch, but does change significantly at $0.4 < z < 1.1$ entirely at $\log(P_{1.4\text{GHz}}) > 10^{25} \text{ W Hz}^{-1}$.

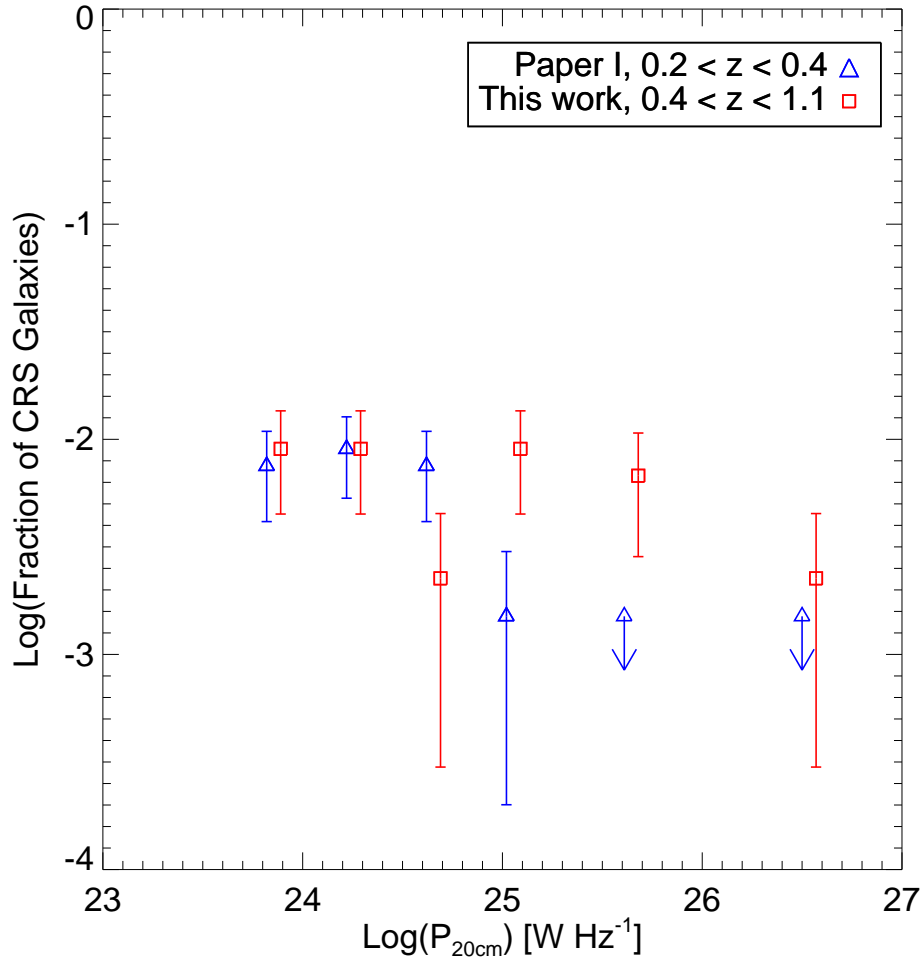


FIG. 8.— Radio luminosity function of radio galaxies in Coma Cluster progenitors between $0.2 < z < 1.1$. The y-axis is the fraction of CRS galaxies located within 1 Mpc of the cluster center that are detected as radio sources within the given radio power bin (refer to Table 8). See §4.1 for details on the calculation of the total number of CRS galaxies. In Coma Cluster progenitors the radio galaxy population at $\log(P_{1.4\text{GHz}}) > 25.0$ W Hz $^{-1}$ evolves from $z \sim 1.1$ to 0.2 with more powerful radio sources situated in less-massive clusters at earlier epochs (3.3σ significance).

6.2. Comparison With Previous High- z Cluster Results

In this sub-section, we compare our RLF results from this work with previous work on high- z cluster radio galaxies by Stocke et al. (1999) and Branchesi et al. (2006). Before the present study, it appeared that the results from those two samples were incompatible. Branchesi et al. (2006) claimed probable density and luminosity evolution of the RLF of cluster radio galaxies between $z \sim 1$ and 0 , while Stocke et al. (1999) claimed no evolution over a similar redshift interval. With the results of this work before us, we hypothesize that both of these results (as well as the current results) are correct and their differences are ascribable to differences in the cluster sample selected for study. Here we compare these three results to see if they are compatible with this hypothesis.

Branchesi et al. (2006) detected 32 radio galaxies in eighteen $0.3 < z < 0.8$ clusters from the ROSAT North Ecliptic Pole (NEP) survey and find potential evidence for evolution in the RLF since $z = 0.8$. Stocke et al. (1999)

find no evolution in the RLF of 21 cluster radio galaxies in 19 EMSS clusters at $0.3 < z < 0.8$ when compared to the RLF of $z < 0.09$ Abell cluster radio sources in Ledlow & Owen (1996). However, EMSS clusters were identified in a flux-limited X-ray sample, which preferentially selects very luminous clusters at high- z . Figure 10 compares the RLF of cluster radio galaxies in this study to the RLF of EMSS radio galaxies. We re-calculated the radio powers of individual EMSS radio galaxies to correct for the different cosmology used in Stocke et al. (1999). The turn-over in the EMSS RLF at $\log(P_{1.4\text{GHz}}) \leq 24.0$ W Hz $^{-1}$ is due to incompleteness at those power levels (Stocke et al. 1999). At $24.0 < \log(P_{1.4\text{GHz}}) < 25.0$ W Hz $^{-1}$, we find that our low- z and combined high- z RLFs are well-matched to the RLF from the EMSS survey (refer to Table 9 and Figure 10). At $\log(P_{1.4\text{GHz}}) > 25.0$ W Hz $^{-1}$, our combined high- z RLF values are larger than those from the EMSS RLF. The EMSS RLF predicts a detection of 0.3 radio galaxies for our combined high- z sample, but we detect 6 radio galaxies (cumulative bino-

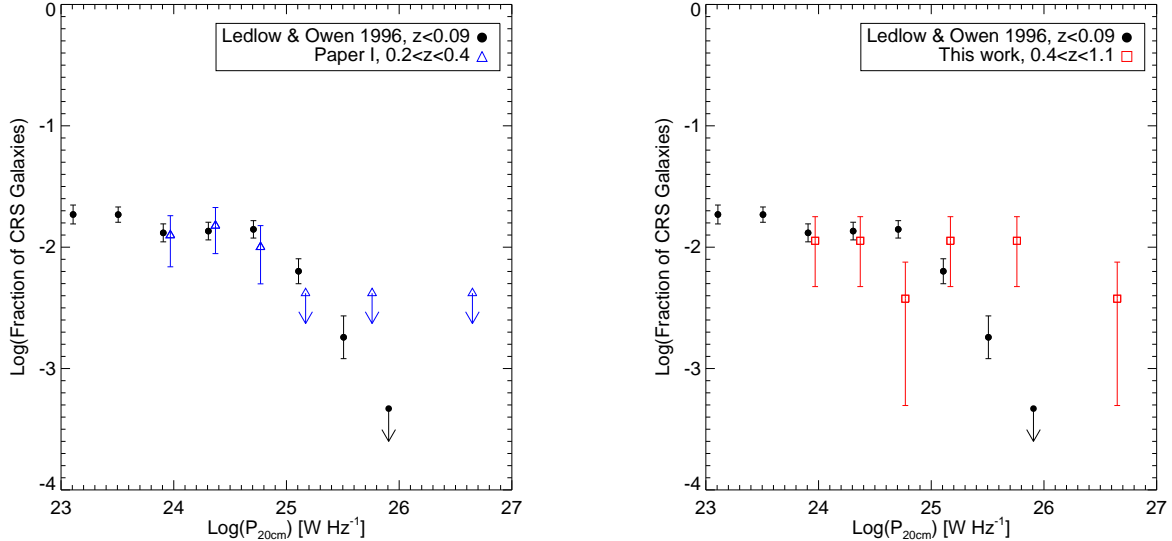


FIG. 9.— RLF comparison between $z < 0.09$ Abell cluster radio galaxies and $0.2 < z < 0.4$ cluster radio galaxies (left) and $0.4 < z < 1.1$ cluster radio galaxies (right). The y-axis is defined as the fraction of CRS galaxies located within 600 kpc of the cluster center (to match the survey area in Ledlow & Owen (1996)) that are detected as radio sources within the given radio power bin. The RLF for our low- z ($0.2 < z < 0.4$) radio galaxies is consistent with the radio galaxy populations in nearby Abell clusters (see Ledlow & Owen 1996). However, the RLF of our sources in clusters at $z > 0.4$ deviates from the nearby Abell clusters at $\log(P_{1.4GHz}) \geq 25.0$ W Hz $^{-1}$.

mial probability of $7 \times 10^{-5}\%$.

There are some major differences between the radio galaxy sample drawn from the NEP and EMSS cluster samples and this current cluster sample. As noted by Branchesi et al. (2006), the mean X-ray luminosity of NEP clusters is lower than that of a typical EMSS cluster, which is twice as luminous as a typical “Road to Coma” progenitor cluster at comparable redshifts. Thus, the more luminous EMSS clusters at high- z have similar masses and X-ray temperatures (see Figure 1) as our low- z clusters, suggesting that EMSS radio galaxies probably reside in similar cluster environments as our low- z radio galaxies. Thus, the “no evolution” conclusion from Stocke et al. (1999) is consistent with our hypothesis that the RLF depends on the cluster sample selection. In conclusion, the results from our internal and external comparisons of the RLF of cluster radio galaxies indicate a significant change in the RLF from $z=0$ – 0.8 in an appropriately chosen sample (see §2). The results presented in this section show that the sample selection of distant clusters does result in finding cluster AGN populations that differ.

7. X-RAY POINT SOURCES IN $0.4 < Z < 1.2$ CLUSTERS

7.1. Statistical XPS Excess Over Background?

Several authors have investigated the statistical XPS excess around clusters of galaxies. Cappelluti et al. (2005) detected XPS over-densities in several clusters, including RXJ0849, RXJ0910, and MS2053, but did not detect over-densities in other cluster fields that overlap with our cluster fields, including RXJ2302, MS1621, and RXJ1113. Cappelluti et al. (2005) suggest that the $>2\sigma$ excess in XPS counts in cluster fields map the filamentary structures ($R \sim 3$ – 5 Mpc) around clusters. These authors note that this XPS excess is statistically insignificant if

larger FOVs are utilized to compute Log N - Log S plots, suggesting that the XPS excess is consistent with the increase of the angular correlation signal at small angular scales. Cappelluti et al. (2005) detect 20–25% variations about their XPS non-cluster reference fields. Due to the small areal coverage in this current work (0.8 deg^{-2}), the differences due to cosmic variance could contribute a similar magnitude of error as Poisson statistics alone.

In a survey of 51 massive clusters from the Massive Cluster Survey (MACS), Ruderman & Ebeling (2005) find a prominent XPS excess within 0.5 Mpc of the cores of clusters with relaxed X-ray morphology, but the XPS excess in MACS clusters with disturbed X-ray morphologies appears more uniformly distributed within a larger 3.5 Mpc survey region. Similarly, within 1 Mpc of 148 galaxy clusters between $0.1 < z < 0.9$, Gilmour et al. (2009) measure a 3σ excess in XPS counts when compared to 44 control fields, resulting in ~ 1.5 XPSs per cluster across their sample. However, these authors find more AGN in the outer 0.5–1.0 Mpc regions than within 0.5 Mpc. Branchesi et al. (2007) find a 2σ excess in the total XPS population within 0.5 Mpc in 18 clusters with $0.25 < z < 1.01$. Six of their clusters overlap with our high- z cluster sample, which includes MS1621, MS2053, RXJ1221, RXJ1350, RXJ1716, WARPSJ1415. Similarly, Martel et al. (2007) find an XPS excess in RXJ0910, RXJ0849, RXJ0152, and MS1054 over most of the soft/hard X-ray bands compared to the observed Log N - Log S plots from the *Chandra* Deep Field North and South. In these large statistical surveys, excess XPSs above the background are assumed to be at the cluster redshift, but little or no redshift information exists to verify cluster membership. Therefore, when redshift information is lacking the evidence for a substantial population of XPSs in clusters is quite mixed.

As stated in §4.2, only $\sim 50\%$ of the detected XPSs in

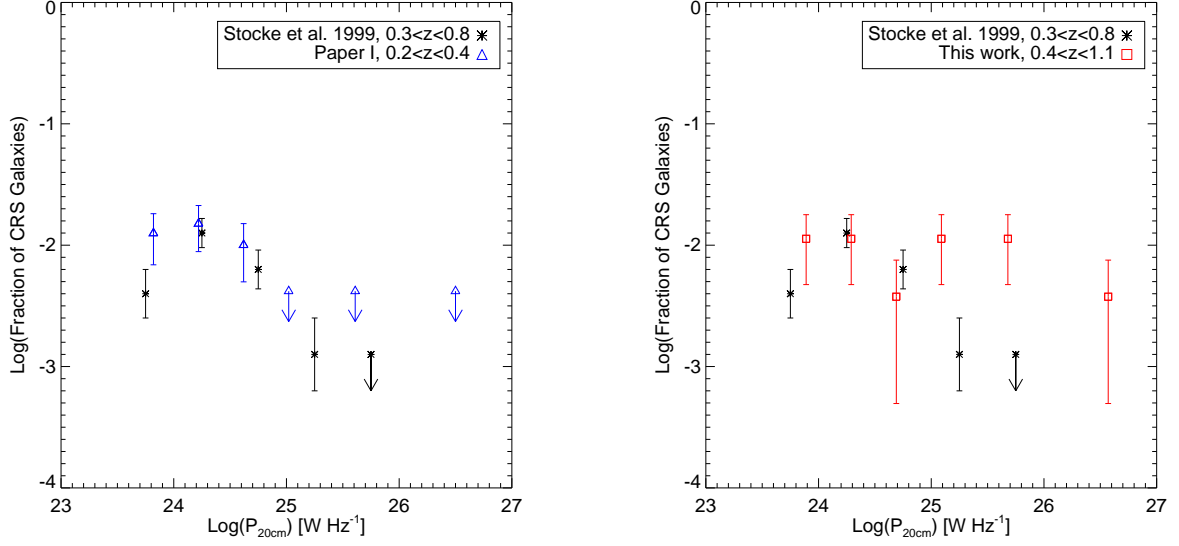


FIG. 10.— RLF comparison between $0.3 < z < 0.8$ EMSS radio galaxies and $0.2 < z < 0.4$ cluster radio galaxies (left) and $0.4 < z < 1.1$ cluster radio galaxies (right). The y-axis is defined as the fraction of CRS galaxies located within 600 kpc of the cluster center (to match the survey area in Stocke et al. (1999)) that are detected as radio sources within the given radio power bin. The RLF for our low- z ($0.2 < z < 0.4$) radio galaxies is consistent with radio galaxies in the flux-limited X-ray sample of massive galaxy clusters in the EMSS (see Stocke et al. 1999). However, the RLF of our cluster radio sources at $z > 0.4$ deviates from the EMSS RLF at $\log(P_{1.4GHz}) > 25.0$ W Hz^{-1} , similar to $0.4 < z < 1.1$ radio source comparisons to the local Abell Cluster radio sources. Clearly, our unique selection of clusters as Coma Cluster progenitors is important to understand the evolution of radio galaxies in cluster environments. EMSS clusters have X-ray luminosities similar to our $0.2 < z < 0.4$ clusters ($L_{0.3-8.0keV} \sim 5 \times 10^{44}$ erg s^{-1}), so it is not surprising that the EMSS RLF is similar to the RLF of our cluster radio galaxies at $0.2 < z < 0.4$.

the present study with $L \geq L^*$ counterparts have known redshifts. This incompleteness hampers any thorough and conclusive analysis of the cluster XPSs at this time. However, the multiwavelength nature of this study provides additional information from the optical and/or radio, as well as results from our low- z sample presented in Paper I, to assess cluster membership. Therefore, in this Section we proceed as far as we can in this analysis with only partial redshift information.

To start, we compare the total number of detected XPSs to the expected background counts to assess the potential number of cluster XPSs at $z > 0.4$ statistically. Using Figure 4 from Kim et al. (2007b), which presents the XPS counts and X-ray background results from ChaMP, we determine the expected number of background XPSs for each cluster's *Chandra* observation within the survey area of 1 Mpc from the cluster center and at X-ray fluxes required to detect cluster XPSs at 5×10^{42} erg s^{-1} at the cluster redshift. However, due to the small survey area of individual cluster observations, we combine the expected numbers into low- z , mid- z , and high- z redshift bins as defined in Table 1. Based on the cosmic X-ray background observations from the X-ray Telescope (XRT) onboard *Swift* (Moretti et al. 2009) and the *Chandra* COSMOS survey (Elvis et al. 2009), we estimate that cosmic variance contributes 20% to the statistical fluctuation in our observed XPS counts and use that amount to compute the total error on the expected number of background XPSs in Table 10.

Table 10 lists the total number of expected background and our detected XPSs at $L_{0.3-8.0keV} \geq 5 \times 10^{42}$ erg s^{-1} if located at the cluster redshift within 1 Mpc of the cluster core for three different redshift bins. This table includes

the number of clusters in each redshift bin, the total survey area, and the cut-off X-ray luminosity at each individual cluster redshift. The statistical significance of the difference between the expected background and our detected XPS counts is listed in Column 7. We find no strong statistical evidence for an XPS excess in our eleven $0.2 < z < 0.4$ cluster fields nor in our five $0.4 < z < 0.8$ cluster fields. These results are consistent with results from ChaMP (Kim et al. 2004), who find no difference in the surface density distribution of XPSs as a function of flux in Log N - Log S plots for *Chandra* fields with and without clusters and no difference in either Log N - Log S when compared to *Chandra* Deep Field measurements of the cosmic X-ray background. In our six $0.8 < z < 1.2$ clusters, we detect a marginal excess of XPSs at $L_{0.3-8.0keV} \geq 5 \times 10^{42}$ erg s^{-1} at the 1.6σ significance level. Therefore, the statistical results from this survey are similar to the ChaMP results and disagree with several earlier studies mentioned previously; i.e., we find no strong evidence for an excess of XPSs in our cluster fields.

7.2. X-ray Active Fraction

In Paper I, we scrutinized the cluster XPS population to determine the nature of those sources. Here we summarize the results from that sample that will be used to compare to the cluster XPSs in our mid- z and high- z clusters fields. At low- z , we detected 12 XPSs at $L_{0.3-8.0keV} \geq 10^{42}$ erg s^{-1} in $L \geq L^*$ galaxies with CRS colors. However, only 6 of those (or 50%) are spectroscopically-confirmed cluster members. Within the same luminosity and magnitude limits, only 1 of 14 XPSs with colors bluer than the CRS (or 7%) is a cluster member (Source A in Figure 2 of Paper I). This one blue

cluster XPS displays the optical properties of a typical Seyfert, $L_{0.3-8.0\text{keV}} = 4.6 \pm 0.1 \times 10^{43} \text{ erg s}^{-1}$ with an X-ray spectrum well-modeled by a power-law with spectral index $\Gamma = 2.0 \pm 0.1$, emission from the 6.4 keV Fe K- α line with an equivalent width of 1.7 keV, and no intrinsic absorption.

Moreover, we identified two cluster XPSs with slight “blue excesses” compared to CRS colors (0.2–0.5 magnitudes bluer than the CRS; See Figure 2 of Paper I). The bluest of these two (Source D in Figure 2 of Paper I) is slightly fainter than M^* . These 2 XPSs have passive optical spectra with no apparent emission lines, and so are very different from the one blue cluster XPS. We suggested that these two passive blue AGN are most similar to low luminosity, X-ray-detected BL-Lacertae (BL Lac) objects that typically have an enhanced blue continuum, which can explain the blue excess (Rector et al. 1999). Recent spectro-polarimetry at the *Subaru* 8m telescope of these two passive blue AGN, confirm the BL Lac classification by detecting continuum polarization (Trump et al. 2011). Because these “passive blue AGN” are most similar to the CRS XPSs rather than the Seyfert-like AGN, we included them in the CRS AGN population.

Based on the detection rate of CRS XPSs per cluster from Paper I, we expect to detect 1–2 XPSs at $L_{0.3-8.0\text{keV}} \geq 5 \times 10^{42} \text{ erg s}^{-1}$ in our combined high- z cluster sample. There are a few candidate sources for passive blue AGN in our high- z clusters (see Figures 3–4), including 2 confirmed cluster members with passive optical spectra (Object C = RXJ1716-X13 and Object D = RXJ0910-X12 in Table 6 and Figure 4). Thus, while not extremely numerous, passive blue AGN do appear to be a new type of cluster active galaxy not identified heretofore. Sources C & D, as well as those few unconfirmed XPSs slightly bluer than the CRS, deserve further scrutiny as potential low-luminosity BL Lac Objects.

At $0.4 < z < 1.2$ we find 62 XPSs in 6 cluster fields with fluxes that correspond to $L_{0.3-8.0\text{keV}} \geq 5 \times 10^{42} \text{ erg s}^{-1}$ at the cluster redshift. From Table 10 the expected number of background XPSs is 44.3 ± 11.1 , so there could be a substantial number of cluster XPSs. We cannot tell without optical spectroscopy, but 7 XPSs listed in Table 6 are spectroscopically-confirmed cluster members (labeled Sources A through G), and all 7 lie on or near the CRS. Thus, at a minimum, these seven CRS XPSs provide a firm *lower* limit of $1.4 \pm 0.8\%$ for the X-ray active fraction (XAF) in clusters at $0.4 < z < 1.2$ and at $L_{0.3-8.0\text{keV}} \geq 5 \times 10^{42} \text{ erg s}^{-1}$. This value is an approximate 10-fold increase compared to the XAF of $0.15 \pm 0.15\%$ for CRS galaxies in our low- z clusters. If, as suggested in Paper I, the CRS XPSs are lower luminosity radio sources, we would expect a similar evolution for the CRS XPSs and the radio galaxies. If confirmed, this increase in the XAF is additional evidence that the radio galaxies and CRS XPSs are members of the same parent population of cluster radio galaxies.

Now we compare our cluster XPS results to Martini et al. (2009), who surveyed 32 galaxy clusters at $0.05 < z < 1.3$ (16 clusters at $0.05 < z < 0.4$ and 15 clusters at $0.4 < z < 1.3$) within the virial radius to investigate the population of luminous $L_{0.3-8.0\text{keV}} > 10^{43} \text{ erg s}^{-1}$ XPSs. Their study found an eight-fold increase in the XAF in

clusters from $0.05 < z < 0.3$ to $0.4 < z < 1.3$. Nine clusters overlap with this work (MS1008, MS1455, MS1358 at $0.2 < z < 0.4$; MS1621, MS2053, RXJ2302 at $0.4 < z < 0.8$; RXJ1716, RXJ0910, RXJ0848 at $0.8 < z < 1.2$). Because Martini et al. (2009) lack photometric catalogs for all of their clusters, they cannot distinguish between red and blue cluster XPSs. So, while we find comparable evolutionary results, there are significant differences in the AGN populations found in these two studies. Martini et al. (2009) have identified numerous broad and narrow emission-line (i.e., Seyfert-like) AGN similar to the one Seyfert we found in our low- z sample mentioned previously. Approximately 50% of the X-ray AGN in Martini et al. (2009) are located within $0.35 R_{200}$, while 45% are located within 0.5 and $1.0 R_{200}$. These emission-line AGN are located well outside the cluster core at a large fraction of R_{200} , while $>50\%$ of our XPSs are CRS absorption-line galaxies close to the cluster core at a few tenths of R_{200} . And while the Martini et al. (2009) sample does contain a few CRS AGN, our sample could contain several Seyfert-like AGN if we had spectroscopy available to confirm them. So, while our evolutionary statistics are broadly consistent in showing a dramatic increase in X-ray active fractions above and below $z \approx 0.4$, these two studies have found two different types of cluster AGN. Further study of both AGN types in high- z clusters clearly are needed. This can be accomplished by obtaining more spectroscopic redshifts for our sample, while two-color imaging and VLA mapping would greatly enhance the Martini et al. (2009) study.

7.3. Cluster Red Sequence XPSs at $z > 0.8$

Seven spectroscopically-confirmed cluster members are detected at $z > 0.8$. These sources are marked with letter identifiers (A-G) in Column 1 of Table 6, in Table 11, and on Figure 4. Sources A-C are located in RXJ1716, Sources D-E are in RXJ0910, and Sources F-G are in RXJ0849. So while there are other candidate CRS X-ray AGN, spectroscopic confirmation is limited to these three well-studied cluster fields. All seven sources have been previously identified by SEXSI (Eckart et al. 2006) and by ChaMP (Kim et al. 2004). Unless otherwise noted, spectral line identifications are provided by Megan Eckart of the SEXSI collaboration.

Sources A-C appear elliptical in our our ARC 3.5m images, as well as in ChaMP images for Source C; Sources D-F appear elliptical in the HST images. In the HST image, Source G is hosted by a galaxy that appears slightly irregular with some “disky” features, even though the host galaxy colors are consistent with the CRS. The host galaxy of Source G has a relative velocity of 2120 km s^{-1} , or 1.6σ from the cluster mean. This XPS may be the BCG of a group of galaxies falling into the main cluster. The optical spectra of these XPSs are typical, passive elliptical galaxy spectra with Ca HK $\lambda 4000$ absorption and weak [O II] $\lambda 3727$ emission. Source A also displays strong [O III] $\lambda 5007$ emission. Source D and Source G are ~ 1.0 and ~ 0.5 magnitudes brighter in the rest-frame Sloan i band than their cluster BCG, as might be expected for clusters “in formation” at high- z .

An eighth potential XPS source, RXJ1350-X7, is coincident with the radio counterpart RXJ1350-R2 (Source 12 in Figure 4). In our ARC 3.5m Sloan (r, i) optical images, two galaxies are located within the 95% encircled

energy radius for this XPS. The best match to the radio AND X-ray source coordinates is the optical source to the SW ($\alpha=13:50:50.1$ and $\delta=60:08:03.8$), which has a smooth appearance in the ARC 3.5m images. Although lacking a redshift, we have counted this object as a cluster radio galaxy in §5. Based upon a limited number of examples, the 7 spectroscopically-confirmed CRS XPSs appear similar in optical morphology and colors to their low- z counterparts, suggesting that they are a similar AGN population to what we found in Paper I.

8. IMPLICATIONS FOR CLUSTER ICM HEATING

Based on our results from §6, we clearly detect evolution in the radio galaxy population in Coma Cluster progenitors from $z=1.1$ to $z=0.2$. In Paper I, we measured an RAF of $2.5 \pm 0.8\%$ for the cluster radio sources and it is $3.8 \pm 1.2\%$ in our combined high- z sample. Referring to the right panel of Figure 5, the radio powers of the BCGs at $0.4 < z < 1.1$ are also larger than the BCGs at $0.2 < z < 0.4$. Cluster radio sources are still hosted by CRS galaxies and $\sim 75\%$ of these radio sources are located within 500 kpc of the cluster core. At $0.4 < z < 0.8$, the cluster radio galaxies remain more centrally concentrated than the CRS galaxies, similar to our results from Paper I. But, at $0.8 < z < 1.1$, cluster radio galaxies do not appear as centrally concentrated, even though their percentage within 500 kpc is similar to those at low- z and mid- z .

In Paper I, we used the scaling relationship between AGN jet power and radio luminosity ($P_{jet} \propto L_r^{0.5}$) from Birzan et al. (2008) to estimate that low-luminosity radio galaxies at $\log(P_{1.4GHz}) \geq 21.4$ W Hz $^{-1}$ contribute $\sim 55\%$ of the total heat input to the ICM. Recently Cavagnolo et al. (2010) extended the Birzan et al. (2008) radio galaxy sample to lower radio power ($L_{1.4GHz} > 10^{21}$ W Hz $^{-1}$ 10^{37} erg s $^{-1}$) and measured a steeper slope of 0.7 for this scaling relationship. With this steeper scaling relationship, we estimate that low-luminosity radio galaxies at $\log(P_{1.4GHz}) \geq 21.4$ W Hz $^{-1}$ contribute $\sim 30\%$ of the total heat input to the ICM, somewhat smaller than our previous estimate.

We now use the updated Cavagnolo et al. (2010) scaling relationship, $P_{jet} \propto L_r^{0.7}$, to estimate the increased jet power per cluster from the enhanced population of FR IIs at $25.0 < \log(P_{1.4GHz}) < 27.0$ W Hz $^{-1}$ in our combined high- z sample. No radio sources at $\log(P_{1.4GHz}) \geq 25.0$ W Hz $^{-1}$ were detected in our low- z cluster sample from Paper I. Using Figure 9, the total integrated radio power per cluster is 3.4×10^{24} W Hz $^{-1}$ at $0.2 < z < 0.4$ and 8.9×10^{25} W Hz $^{-1}$ at $0.4 < z < 1.1$, approximately $26\times$ higher than the integrated luminosity in Coma Cluster progenitors at $0.2 < z < 0.4$. This increase in radio power per cluster corresponds to a 9–10 fold increase in the integrated jet power and thus more heat is predicted to be available for deposition into the surrounding ICM by these radio jets. Figure 7 shows an excellent example of a high- z ($z = 0.8$) cluster from our sample in which three luminous radio galaxies are found, including in the BCG. However, the most luminous by-far is well-offset from the cluster center and so can provide significant ICM heating which is both off-center and mobile with respect to the intra-cluster gas. A large majority (75%) of cluster radio galaxies at $z > 0.4$ are located within 500 kpc, so the ad-

ditional sources of heating, at higher radio powers, will be concentrated in the inner ICM regions as well.

The impact of cluster XPSs on the heating of the ICM is more difficult to assess due to the spectroscopic incompleteness of our sample, but is likely much less than the radio galaxy population. Both this paper and Martini et al. (2009) find a marked increase in the X-ray active fraction in higher redshift clusters, comparable to the increase in the radio galaxy active fractions. The increase we have found is in the CRS AGN population close to the cluster core, which we have ascribed to low luminosity BL Lac Objects and thus to quite weak radio jets. Martini et al. (2009) find this increase predominantly in Seyfert-like AGN which are much further from the cluster center, near R_{200} (although these authors do identify a few absorption line AGN close to the cluster centers as well). The heat input provided by Seyfert-like (i.e., radio-quiet) AGN is not well-known or measured (e.g., Arav et al. 2002), but any heat they provide would be well outside the dense ICM region. Therefore, the radio galaxies provide the bulk of the ICM heat input and so the analysis outlined above provides strong evidence for a greatly increased heat input to higher- z cluster ICM gas. But, based on the current work and Martini et al. (2009), there is still much work to be done to better characterize the ICM heat input, including a more complete census of the absorption and emission-line AGN in high- z clusters and their radial distribution relative to the ICM. Theoretical work which models the heat input by non-central, moving AGN sources embedded in an evolving, less dense ICM are needed to assess the efficiency of such input as a function of redshift.

9. SUMMARY AND CONCLUSIONS

As a companion paper to Hart et al. (2009, Paper I), we have presented an extensive investigation of the multiwavelength nature of AGN in a sample of 22 clusters of galaxies at $0.2 < z < 1.2$, specifically chosen to be most similar to Coma Cluster progenitors at those redshifts. Using the X-ray temperature of the ICM as a proxy for cluster mass, we chose massive clusters (or high X-ray temperature clusters) at lower redshifts and less massive clusters (or lower X-ray temperature clusters) at higher redshifts to investigate the X-ray point source (XPS) and radio galaxy populations. In both wavelength regimes, the limiting luminosities were chosen to sample only the AGN populations in $L \geq L^*$ galaxies.

Within 1 Mpc of the cluster center, we detect 19 radio galaxies at $P_{1.4GHz} \geq 5 \times 10^{23}$ W Hz $^{-1}$ in our $0.4 < z < 1.2$ clusters (11 of which are spectroscopically-confirmed cluster members and 8 of which are likely cluster members because they have colors similar to the cluster red sequence (CRS). Because 8 CRS AGN do not have confirming spectroscopic redshifts, we conservatively reduce the total number of radio galaxies in this sample by 2 to 17 based upon the foreground/background AGN contamination we found within the bounds of the CRS in Paper I. Similarly, we detect 7 spectroscopically-confirmed cluster XPSs. Both the X-ray and radio AGN have host galaxies with colors consistent with CRS galaxies. There is some evidence that the radio galaxies become more centrally concentrated in these clusters at lower redshift. Among the radio galaxies we have found a clear FR II morphology source at $z=0.8$ with $P_{1.4GHz} = 7.7 \times 10^{26}$ W

Hz^{-1} , while no FR IIs were detected at $P_{1.4\text{GHz}} > 10^{25} \text{ W Hz}^{-1}$ in our low- z sample. In addition to this one luminous FR-II, we detect several other radio galaxies at $P_{1.4\text{GHz}} > 10^{25} \text{ W Hz}^{-1}$ in our $z > 0.4$ clusters, including several BCGs. These sources are all more powerful than any we found at low- z .

While previous work (e.g., Ellingson et al. 1991; Hill & Lilly 1991; Harvanek & Stocke 2002) has discovered clusters of galaxies around clear FR II morphology and power level sources at $z > 0.4$, here we started with rich clusters at those redshifts and have discovered an FR II. Therefore, there is no doubt that the morphology and power level of some cluster radio galaxies is changing between $z=1$ and 0. Specifically, this study provides further support for a phenomenological model in which the power levels of subsequent outbursts of radio galaxies in clusters diminishes rapidly between these redshifts (Ellingson et al. 1991; Harvanek & Stocke 2002), the same range of redshifts over which the ICM density and temperature dramatically increase (see Figure 1). Evidence presented herein and in Paper I that radio galaxies are more centrally concentrated in their clusters than the CRS elliptical galaxy population as a whole is further evidence for a link between AGN activity and ICM density (see also Stocke & Perrenod 1981). It is possible that this AGN/ICM relationship may provide the necessary negative feedback mechanism to prevent runaway cooling in cluster cores (e.g., McCarthy et al. 2008).

A comparison between the RLF of our $0.2 < z < 0.4$ radio sources versus those in our $0.4 < z < 1.2$ sample reveals a larger number of high-power sources at earlier epochs, evidence for positive evolution of these sources in Coma Cluster progenitors. A comparison between the RLF of our $0.2 < z < 0.4$ cluster radio sources to local ($z < 0.09$) Abell cluster radio sources shows that the two populations are similar, suggesting little evolution between $0.2 < z < 0.4$ and $z=0$. The clear density and luminosity evolution of radio galaxies found in our sample of cluster AGN is quite different from the absence of evolution found by Stocke et al. (1999) using a flux-limited sample of EMSS clusters. We interpret this lack of agreement as support for our novel, physically-based method for selecting clusters for study, the “Road to Coma” concept presented in the §2. We suggest that both AGN evolution results are correct and that Stocke et al. (1999) failed to find cluster AGN evolution because their high- z sample has very similar ICM properties to the low- z sample of Ledlow & Owen (1996), to which they compared AGN populations. For example, the hot, $z=0.8$ cluster, MS 1045-03 (see Figure 1) is a member of the Stocke et al. (1999) high- z sample and has a similar radio galaxy population to many $z=0$ rich Abell clusters. Our sample was selected to avoid that pitfall and we conclude that sample selection is as critical for cluster galaxy and AGN studies as it is for other evolutionary investigations.

We can be far less definitive concerning the evolu-

tion of cluster X-ray AGN due to the large number of XPSs in our high- z cluster fields and to the absence of redshift information for most of them. However, there are sufficient redshifts (7) for CRS XPSs to show that the passive, absorption-line AGN population that was identified in Paper I persists at high- z . Although the statistics are quite sparse, a substantial increase in either the density and/or the luminosity of this AGN class (at least an order of magnitude increase in active fraction at $L_{0.3-8.0\text{keV}} \geq 5 \times 10^{42} \text{ erg s}^{-1}$ when compared to low- z) is very similar to the rapid increase recently found in the cluster X-ray AGN population by Martini et al. (2009).

However, our study is more complementary to this previous study than confirming because different AGN classes are involved. Optical spectroscopy, primarily derived from the SEXSI study, and deep ground-based and HST imaging for our CRS XPSs finds that these passive AGN are hosted in rather normal, giant elliptical galaxies positioned rather close to the cluster core, whereas the Martini et al. (2009) AGN are largely emission-line galaxies similar to Seyferts found further out in the clusters near R_{200} . Since the energy and mass outflow from Seyferts (i.e., radio-quiet AGN population) is still not well-measured (Arav et al. 2002), it is not known whether these AGN contribute significantly to ICM heating or not.

Paper I identified the CRS XPSs as low-luminosity BL Lac Objects, suggesting that they possess relativistic jets. But the absence of radio emission from these sources suggest that these jets are too weak to inject much heat into the ICM (see Paper I for details). However, these CRS X-ray AGN are worthy of further study since deep X-ray imaging (e.g., Barger et al. 2001) finds that a substantial fraction ($\sim 20\%$) of the faint XPS population is due to passive AGN like these cluster sources. So their detailed nature and cosmological evolution is of considerable interest.

Using the recent scaling law between AGN jet power and the radio luminosity suggested by Cavagnolo et al. (2010), $P_{\text{jet}} \propto L_r^{0.7}$, we determine that the excess power from luminous radio galaxies at $23 < \log(P_{1.4\text{GHz}}) < 27 \text{ W Hz}^{-1}$ is $\sim 26\times$ higher in $0.4 < z < 1.1$ clusters than in $0.2 < z < 0.4$ clusters, which corresponds to 9–10 fold increase in the AGN jet power if FR II jets have similar kinetic energies to FR I jets. Using the more shallow scaling between AGN jet power and the radio luminosity from Birzan et al. (2008) corresponds to a 5–6 fold increase. Therefore, a larger amount of heat can be deposited into the ICM at high- z . The results presented herein and by previous studies of AGN in high- z clusters (e.g., Ellingson et al. 1991; Hill & Lilly 1991; Harvanek & Stocke 2002; Martini et al. 2009) invites new theoretical work on the co-evolution of AGN and the cluster ICM and its effect on ICM heating and cooling.

APPENDIX

DETECTED XPSs IN $0.4 < z < 1.2$ CLUSTERS

This section contains Table 11, a complete list of detected XPSs in our $0.4 < z < 1.2$ clusters listed in Table 1. These XPSs, if located at the cluster redshift, are at $L_{0.3-8.0\text{keV}} \geq 5 \times 10^{42} \text{ erg s}^{-1}$ and are located at a projected distance less than 1 Mpc from the cluster X-ray emission centroid (see Columns 2-3 of Table 2). For completeness we include the

sources from Table 6, which lists only the spectroscopically-confirmed cluster XPSs within the above limits.

QNH and JTS acknowledge the support from the *Chandra* Theory/Archive Grant AR8-9013X. AEE acknowledges support from NSF AST-0708150 and NASA NNX10AF61G. We thank Brian Keeney for assistance with our optical observations, Yasuhiro Hashimoto for providing use of the Subaru images of RXJ1053, Eric Perlman and Harald Ebeling of the WARPS collaboration for providing 1.4 GHz maps and spectroscopic information, and Megan Eckart for providing us with detailed spectral line identifications of X-ray AGN in clusters that overlap with the SEXSI study. QNH acknowledges useful conversation with Jack Burns and Eric Hallman.

We would like to acknowledge Paul Green and the *Chandra* Multi-wavelength Project (ChaMP; Green et al. 2004) collaboration for providing use of the their photometric datasets on some cluster fields. ChaMP is supported by NASA. Optical data for ChaMP are obtained in part through NOAO, operated by the Association of Universities for Research in Astronomy, Inc. (AURA), under cooperative agreement with the National Science Foundation.

Funding for the SDSS and SDSS-II has been provided by the Alfred P. Sloan Foundation, the Participating Institutions, the National Science Foundation, the U.S. Department of Energy, the National Aeronautics and Space Administration, the Japanese Monbukagakusho, the Max Planck Society, and the Higher Education Funding Council for England. The SDSS Web Site is <http://www.sdss.org/>. This research has made use of data obtained from the *Chandra* Data Archive and software provided by the *Chandra* X-ray Center (CXC) in the application packages CIAO, ChIPS, and Sherpa.

Some of the data presented in this paper were obtained from the Multimission Archive at the Space Telescope Science Institute (MAST). STScI is operated by the Association of Universities for Research in Astronomy, Inc., under NASA contract NAS5-26555. Support for MAST for non-HST data is provided by the NASA Office of Space Science via grant NNX09AF08G and by other grants and contracts.

This research has made use of the NASA/IPAC Extragalactic Database (NED) which is operated by the Jet Propulsion Laboratory, California Institute of Technology, under contract with the National Aeronautics and Space Administration, as well as NASA's Astrophysics Data System.

Facilities: CXO, ARC (3.5m), VLA, Sloan, HST

REFERENCES

- Adelman-McCarthy, J. K., et al. 2008, *ApJS*, 175, 297
 Arav, N., Korista, K. T., & de Kool, M. 2002, *ApJ*, 566, 699
 Barger, A. J., Cowie, L. L., Mushotzky, R. F., & Richards, E. A. 2001, *AJ*, 121, 662
 Becker, R. H., White, R. L., & Helfand, D. J. 1995, *ApJ*, 450, 559
 Bell, E. F., et al. 2004, *ApJ*, 608, 752
 Bertin, E., & Arnouts, S. 1996, *A&AS*, 117, 393
 Best, P. N., von der Linden, A., Kauffmann, G., Heckman, T. M., & Kaiser, C. R. 2007, *MNRAS*, 379, 894
 Bialek, J. J., Evrard, A. E., & Mohr, J. J. 2001, *ApJ*, 555, 597
 Birzan, L., McNamara, B. R., Nulsen, P. E. J., Carilli, C. L., & Wise, M. W. 2008, *ApJ*, 686, 859
 Blakeslee, J. P., et al. 2006, *ApJ*, 644, 30
 Borgani, S., et al. 2004, *MNRAS*, 348, 1078
 Bower, R. G., et al. 2006, *MNRAS*, 370, 645
 Branchesi, M., Gioia, I. M., Fanti, C., Fanti, R., & Cappelluti, N. 2007, *A&A*, 462, 449
 Branchesi, M., Gioia, I. M., Fanti, C., Fanti, R., & Perley, R. 2006, *A&A*, 446, 97
 Brüggen, M., Ruszkowski, M., & Hallman, E. 2005, *ApJ*, 630, 740
 Brüggen, M., Scannapieco, E., & Heinz, S. 2009, *MNRAS*, 395, 2210
 Bruzual, G., & Charlot, S. 2003, *MNRAS*, 344, 1000
 Burns, J. O. 1990, *AJ*, 99, 14
 Capak, P., et al. 2007, *ApJS*, 172, 99
 Cappelluti, N., et al. 2005, *A&A*, 430, 39
 Cavagnolo, K. W., et al. 2010, *ApJ*, 720, 1066
 Cohen, A. S., et al. 2007, *AJ*, 134, 1245
 Constantin, A., et al. 2009, *ApJ*, 705, 1336
 Cooray, A. R., Grego, L., Holzapfel, W. L., Joy, M., & Carlstrom, J. E. 1998, *AJ*, 115, 1388
 Demarco, R., et al. 2005, *A&A*, 432, 381
 Dickey, J. M., & Lockman, F. J. 1990, *ARA&A*, 28, 215
 Dressler, A., Oemler, A. J., Sparks, W. B., & Lucas, R. A. 1994, *ApJ*, 435, L23
 Ebeling, H., Edge, A. C., & Henry, J. P. 2001, *ApJ*, 553, 668
 Eckart, M. E., et al. 2006, *ApJS*, 165, 19
 Ellingson, E., Yee, H. K. C., & Green, R. F. 1991, *ApJ*, 371, 49
 Ellis, R. S., et al. 1997, *ApJ*, 483, 582
 Elvis, M., et al. 2009, *ApJS*, 184, 158
 Evrard, A. E. 1988, *MNRAS*, 235, 911
 Evrard, A. E., et al. 2002, *ApJ*, 573, 7
 Fabian, A. C., Celotti, A., Blundell, K. M., Kassim, N. E., & Perley, R. A. 2002, *MNRAS*, 331, 369
 Finoguenov, A., et al. 2004, *A&A*, 419, 47
 Fukugita, M., Shimasaku, K., & Ichikawa, T. 1995, *PASP*, 107, 945
 Gehrels, N. 1986, *ApJ*, 303, 336
 Gilmour, R., Best, P., & Almaini, O. 2009, *MNRAS*, 392, 1509
 Gioia, I. M., Henry, J. P., Mullis, C. R., Ebeling, H., & Wolter, A. 1999, *AJ*, 117, 2608
 Gioia, I. M., & Luppino, G. A. 1994, *ApJS*, 94, 583
 Gladders, M. D., & Yee, H. K. C. 2005, *ApJS*, 157, 1
 Green, P. J., et al. 2004, *ApJS*, 150, 43
 Haggard, D., et al. 2010, *ApJ*, 723, 1447
 Hallman, E. J., et al. 2007, *ApJ*, 671, 27
 Harrison, F. A., Eckart, M. E., Mao, P. H., Helfand, D. J., & Stern, D. 2003, *ApJ*, 596, 944
 Hart, Q. N., Stocke, J. T., & Hallman, E. J. 2009, *ApJ*, 705, 854
 Harvanek, M., Ellingson, E., Stocke, J. T., & Rhee, G. 2001, *AJ*, 122, 2874
 Harvanek, M., & Stocke, J. T. 2002, *AJ*, 124, 1239
 Hashimoto, Y., Henry, J. P., Hasinger, G., Szokoly, G., & Schmidt, M. 2005, *A&A*, 439, 29
 Hasinger, G., et al. 1998, *A&A*, 340, L27
 Heinz, S., Brüggen, M., Young, A., & Levesque, E. 2006, *MNRAS*, 373, L65
 Henry, J. P., et al. 1997, *AJ*, 114, 1293
 Hill, G. J., & Lilly, S. J. 1991, *ApJ*, 367, 1
 Holden, B. P., et al. 2006, *ApJ*, 642, L123
 Hornschemeier, A. E., et al. 2006, *ApJ*, 643, 144
 Jee, M. J., et al. 2006, *ApJ*, 642, 720
 Kim, D., et al. 2006, *ApJ*, 644, 829
 Kim, D.-W., et al. 2004, *ApJ*, 600, 59
 Kim, M., et al. 2007a, *ApJS*, 169, 401
 —. 2007b, *ApJ*, 659, 29
 Koester, B. P., et al. 2007, *ApJ*, 660, 239
 Ledlow, M. J., & Owen, F. N. 1995, *AJ*, 110, 1959
 —. 1996, *AJ*, 112, 9
 Lewis, A. D., Stocke, J. T., Ellingson, E., & Gaidos, E. J. 2002, *ApJ*, 566, 744
 Lin, Y.-T., & Mohr, J. J. 2007, *ApJS*, 170, 71
 Lutovinov, A. A., Vikhlinin, A., Churazov, E. M., Revnivtsev, M. G., & Sunyaev, R. A. 2008, *ApJ*, 687, 968
 Martel, A. R., Menanteau, F., Tozzi, P., Ford, H. C., & Infante, L. 2007, *ApJS*, 168, 19
 Martini, P., Sivakoff, G. R., & Mulchaey, J. S. 2009, *ApJ*, 701, 66
 Mateos, S., et al. 2005, *A&A*, 444, 79
 McCarthy, I. G., Babul, A., Bower, R. G., & Balogh, M. L. 2008, *MNRAS*, 386, 1309
 McNamara, B. R., & O'Connell, R. W. 1989, *AJ*, 98, 2018
 —. 1993, *AJ*, 105, 417
 Mei, S., et al. 2006a, *ApJ*, 639, 81
 —. 2006b, *ApJ*, 644, 759

- Miley, G. K., Perola, G. C., van der Kruit, P. C., & van der Laan, H. 1972, *Nature*, 237, 269
- Miller, N. A., et al. 2009, *AJ*, 137, 4450
- Monet, D. G., et al. 2003, *AJ*, 125, 984
- Moretti, A., et al. 2009, *A&A*, 493, 501
- Muller, G. P., Reed, R., Armandroff, T., Boroson, T. A., & Jacoby, G. H. 1998, *Proc. SPIE*, 3355, 577
- Mullis, C. R., et al. 2003, *ApJ*, 594, 154
- Nagai, D., Kravtsov, A. V., & Vikhlinin, A. 2007, *ApJ*, 668, 1
- Newberg, H. J., Richards, G. T., Richmond, M., & Fan, X. 1999, *ApJS*, 123, 377
- O'Dea, C. P., & Owen, F. N. 1986, *ApJ*, 301, 841
- O'Neill, S. M., & Jones, T. W. 2010, *ApJ*, 710, 180
- Peacock, J. A. 1999, *Cosmological Physics*, ed. Peacock, J. A.
- Perlman, E. S., et al. 2002, *ApJS*, 140, 265
- Pesce, J. E., Fabian, A. C., Edge, A. C., & Johnstone, R. M. 1990, *MNRAS*, 244, 58
- Peterson, J. R., et al. 2003, *ApJ*, 590, 207
- Ponman, T. J., Cannon, D. B., & Navarro, J. F. 1999, *Nature*, 397, 135
- Postman, M., et al. 2005, *ApJ*, 623, 721
- Pratt, G. W., et al. 2007, *A&A*, 461, 71
- Press, W., Flannery, B., Teukolsky, S., & Vetterling, W. 1992, *Numerical Recipes in C: The Art of Scientific Computing* (Cambridge University Press)
- Rector, T. A., Stocke, J. T., & Perlman, E. S. 1999, *ApJ*, 516, 145
- Rosati, P., della Ceca, R., Norman, C., & Giacconi, R. 1998, *ApJ*, 492, L21+
- Ruderman, J. T., & Ebeling, H. 2005, *ApJ*, 623, L81
- Ruszkowski, M., Brüggem, M., & Begelman, M. C. 2004, *ApJ*, 611, 158
- Sarazin, C. L. 1986, *Reviews of Modern Physics*, 58, 1
- Schindler, S., & Wambsganss, J. 1996, *A&A*, 313, 113
- Schlegel, D. J., Finkbeiner, D. P., & Davis, M. 1998, *ApJ*, 500, 525
- Schneider, D. P., et al. 2002, *AJ*, 123, 567
- Silverman, J. D., et al. 2005, *ApJ*, 618, 123
- Springel, V., et al. 2005, *Nature*, 435, 629
- Stanford, S. A., Eisenhardt, P. R., & Dickinson, M. 1998, *ApJ*, 492, 461
- Stanford, S. A., et al. 2002, *AJ*, 123, 619
- Stern, D., et al. 2002, *AJ*, 123, 2223
- Stocke, J. T., Perlman, E. S., Gioia, I. M., & Harvanek, M. 1999, *AJ*, 117, 1967
- Stocke, J. T., & Perrenod, S. C. 1981, *ApJ*, 245, 375
- Trump, J. R., et al. 2011, *ApJ*, 732, 23
- van Dokkum, P. G., & van der Marel, R. P. 2007, *ApJ*, 655, 30
- Vernaleo, J. C., & Reynolds, C. S. 2007, *ApJ*, 671, 171
- Visvanathan, N., & Sandage, A. 1977, *ApJ*, 216, 214
- Wechsler, R. H., Bullock, J. S., Primack, J. R., Kravtsov, A. V., & Dekel, A. 2002, *ApJ*, 568, 52
- White, R. L., & Becker, R. H. 1992, *ApJS*, 79, 331
- Yasuda, N., et al. 2001, *AJ*, 122, 1104
- Yee, H. K. C. 1991, *PASP*, 103, 396
- Yee, H. K. C., Ellingson, E., & Carlberg, R. G. 1996, *ApJS*, 102, 269
- Yee, H. K. C., Green, R. F., & Stockman, H. S. 1986, *ApJS*, 62, 681
- Zappacosta, L., et al. 2005, *A&A*, 434, 801

TABLE 1
THE “ROAD TO COMA” SAMPLE: 23 GALAXY CLUSTERS BETWEEN $0.2 < z < 1.2$

Redshift Bin (1)	No. of Clusters (2)	Cluster Name (3)	z (4)	kT (keV) (5)
0.2 < z < 0.4 (Low- z)	11	MS 0440.5+0204	0.197	$6.1^{+0.6}_{-0.5}$
		Abell 963	0.206	$7.1^{+0.2}_{-0.2}$
		RX J0952.8+5153	0.214	$5.2^{+0.2}_{-0.2}$
		Abell 2111	0.229	$7.2^{+0.6}_{-0.5}$
		MS 1455.0+2232	0.260	$4.5^{+0.1}_{-0.1}$
		Abell 1758	0.280	$7.5^{+0.5}_{-0.3}$
		MS1008.1-1224	0.306	$6.1^{+0.4}_{-0.5}$
		MS2137.3-2353	0.313	$4.6^{+0.1}_{-0.1}$
		Abell 1995	0.319	$8.8^{+0.5}_{-0.5}$
		MS1358.4+6245	0.330	$8.2^{+0.7}_{-0.7}$
		Abell 370	0.373	$8.5^{+0.5}_{-0.5}$
0.4 < z < 0.8 (Mid- z)	5	MS 1621.5+2640	0.426	$6.2^{+0.7}_{-0.6}$
		MS 2053.7-0449	0.587	$4.5^{+1.0}_{-0.7}$
		RX J1221.4+4918	0.700	$6.9^{+0.7}_{-0.7}$
		RX J2302.8+0844	0.720	$7.4^{+2.4}_{-1.0}$
		RX J1113.1-2615	0.725	$5.6^{+1.7}_{-1.0}$
0.8 < z < 1.2 (High- z)	7	RX J1350.0+6007	0.796	$4.5^{+0.9}_{-0.7}$
		RX J1716.6+6708	0.809	$6.7^{+1.0}_{-0.9}$
		RX J0152.7-1357 ^a	0.835	$5.0^{+0.7}_{-0.7}$
		WARPS J1415.1+3611	1.013	$5.1^{+0.6}_{-0.5}$
		RX J0910.7+5422	1.106	$5.3^{+3.7}_{-1.7}$
		RX J1053.7+5735	1.134	$3.3^{+0.7}_{-0.6}$
		RX J0848.9+4452	1.260	$3.4^{+2.1}_{-0.8}$

NOTE. — Columns: (1) Redshift bin (2) Number of clusters in this redshift bin (3) Cluster name (4) Redshift (5) Bulk X-ray temperature of the intracluster medium. See § 3.1 for details.

^a The X-ray emission of RXJ0152 is double-peaked. The quoted bulk ICM temperature is extracted from a region that includes a 500 kpc radius around EACH X-ray clump. The resulting extraction radius is 900 kpc. The individual X-ray temperature within 500 kpc of the clump centers is $5.6^{+1.0}_{-0.7}$ for the North clump and $5.2^{+0.7}_{-0.7}$ for the South clump.

TABLE 2
Chandra X-RAY OBSERVATIONS OF TWELVE $0.4 < z < 1.2$ CLUSTERS

Cluster	RA	DEC	<i>Chandra</i> ObsID	ACIS Chip	Exp. Time (ksec)	F_X^{limit} $\times 10^{-15}$	L_X^{limit} $\times 10^{41}$
(1)	(2)	(3)	(4)	(5)	(6)	(7)	(8)
MS 1621.5+2640	16:23:35.3	+26:34:20.6	546	I3	29.9	3.2	2.1
MS 2053.7-0449	20:56:21.4	-04:37:49.1	1667	I3	43.9	0.8	2.3
RX J1221.4+4918	12:21:26.4	+49:18:26.8	1662	I3	78.5	1.3	2.8
RX J2302.8+0844	23:02:48.2	+08:43:51.2	918	I3	107.6	0.8	1.8
RX J1113.1-2615 ^a	11:13:05.3	-26:15:39.8	915	I3	104.6	1.0	2.5
RX J1350.0+6007 ^b	13:50:48.3	+60:07:10.8	2229	I3	57.9	1.4	4.2
RX J1716.6+6708 ^b	17:16:48.9	+67:08:23.0	548	I3	51.5	1.6	5.0
RX J0152.7-1357 ^c	01:52:42.0	-13:58:01.0	913	I3	36.3	2.5	7.5*
WARPS J1415.1+3611 ^b	14:15:11.2	+36:12:01.5	4163	I3	88.8	0.9	4.9
RX J0910.7+5422 ^{b,d}	09:10:45.0	+54:22:03.7	2227	I3	105.1	0.8	5.1
RX J1053.7+5735 ^{b,d}	10:53:39.9	+57:35:16.9	4936	S3	88.4	0.7	4.6
RX J0848.9+4452 ^{b,d}	08:48:58.7	+44:51:52.5	927,1708	I2	185.1	0.5	4.8

NOTE. — Columns: (1) Cluster name (2-3) RA and DEC (J2000) of the ICM emission centroid based on 2D elliptical Gaussian profile fits. (4) *Chandra* observation ID (5) ACIS aimpoint (6) Exposure time of the observation after filtering for flaring events (7) X-ray flux limit (0.3-8.0 keV) in $\text{erg cm}^{-2} \text{s}^{-1}$ for a point source near the edge of our survey region ($R=1$ Mpc). See § 3.1 for more details. (8) K-corrected X-ray luminosity limit (0.3-8.0 keV) in erg s^{-1} for the flux limits in Column 7.

* Although the X-ray luminosity limit for this cluster is $L_{0.3-8.0\text{keV}} \geq 5.0 \times 10^{42} \text{ erg s}^{-1}$, RXJ0152 is included in radio-related statistics in the later sections because the 1.4 GHz radio map detects sources at $P_{1.4\text{GHz}} > 1.3 \times 10^{23} \text{ W Hz}^{-1}$.

^a The ICM spectrum was extracted between 0.5–6.0 keV.

^b The ICM spectrum was extracted within a 500 kpc radius from the cluster core.

^c The X-ray emission of RXJ0152 is double-peaked and this coordinate is approximately between the peaks.

^d The ICM spectrum was binned to a minimum of 40 counts per bin prior to XSPEC model fitting.

TABLE 3
 1.4 GHz OBSERVATIONS OF TWELVE $0.4 < z < 1.2$ CLUSTERS

Cluster Name	VLA 1.4 GHz Map	$S_{1.4,lim}$ (mJy/Beam)	$P_{1.4,lim}$ ($\times 10^{23}$)	$L_{1.4,lim}$ ($\times 10^{39}$)
(1)	(2)	(3)	(4)	(5)
MS 1621.5+2640 ^a	AP245 (A)	0.14	0.8	1.1
MS 2053.7-0449	AP219 (B)	0.18	2.2	3.1
RX J1221.4+4918	AS873 (B)	0.11	2.0	2.8
RX J2302.8+0844	AP422 (B)	0.18	3.5	5.0
RX J1113.1-2615	AS873 (AB)	0.11	2.2	3.1
RX J1350.0+6007	AS873 (B)	0.14	3.6	5.0
RX J1716.6+6708	AS873 (B)	0.16	4.2	5.8
RX J0152.7-1357	AC757 (A)	0.15	4.2	5.9
	AL713 (B)	0.45	12.6	17.6
WARPS J1415.1+3611	AP439 (B)	0.03	1.3	1.8
RX J0910.7+5422 ^b	AS873 (B)	0.21	11.3	15.7
RX J1053.7+5735	AC587 (B)	0.03	1.7	2.4
RX J0848.9+4452 ^b	AB1036 (AB)	0.18	13.0	18.3

NOTE. — Columns: (1) Cluster name (2) VLA program ID with the array configuration in parentheses (3) 1.4 GHz radio flux density limit in mJy/Beam and (4) radio power limit in W Hz^{-1} and (5) radio luminosity limit at 1.4 GHz in erg s^{-1} for a 3σ detection at the edge of our survey region.

^a FIRST detects sources at $P_{1.4\text{GHz}} > 2.3 \times 10^{23} \text{ W Hz}^{-1}$ or $L_{1.4\text{GHz}} > 3.2 \times 10^{39} \text{ erg s}^{-1}$ for this cluster.

^b This cluster is excluded from radio-related statistics because the radio power limit is $P_{1.4\text{GHz}} \geq 5 \times 10^{23} \text{ W Hz}^{-1}$.

TABLE 4
 OPTICAL IMAGES OF TWELVE $0.4 < z < 1.2$ CLUSTERS

Cluster	Color	CRS Color Observed	Expected	m_{lim}	m^*	N_{CRS}	Survey Images
(1)	(2)	(3)	(4)	(5)	(6)	(7)	(8)
MS 1621.5+2640	Sloan (r-i)	0.66 ± 0.10	0.89	$(r,i) = (22.2, 21.3)$	$r = 21.4$	36	SDSS DR6
MS 2053.7-0449	Sloan (r-i)	1.27 ± 0.15	1.14	$(r,i) = (24.8, 24.2)$	$r = 22.5$	29	ChaMP
RX J1221.4+4918	Sloan (r-i)	1.27 ± 0.27	1.32	$(r,i) = (24.0, 23.2)$	$r = 23.8$	52	ARC 3.5m, 2006
RX J2302.8+0844	Sloan (r-i)	1.31 ± 0.27	1.35	$(r,i) = (25.5, 24.6)$	$r = 24.0$	27	ChaMP
RX J1113.1-2615	Sloan (r-i)	1.41 ± 0.24	1.35	$(r,i) = (25.8, 25.1)$	$r = 24.0$	31	ChaMP
RX J1350.0+6007	Sloan (r-i)	1.12 ± 0.21	1.46	$(r,i) = (24.7, 24.0)$	$r = 24.2$	37	ARC 3.5m, 2006
RX J1716.6+6708	Sloan (r-i)	1.30 ± 0.15	1.47	$(r,i) = (23.8, 23.5)$	$r = 23.5$	56	ARC 3.5m, 2006
RX J0152.7-1357	(F625W-F775W)	1.20 ± 0.30	1.47	$(i,z) = (27.1, 27.0)$	$i = 22.9$	49	<i>HST</i> ACS WFC, Program 9290
WARPS J1415.1+3611	(F775W-F850LP)	0.90 ± 0.31	$\sim 1.0^a$	$(i,z) = (26.8, 27.0)$	$i = 23.9$	52	<i>HST</i> ACS WFC, Program 10496
RX J0910.7+5422	(F775W-F850LP)	0.93 ± 0.32	$\sim 1.0^a$	$(i,z) = (26.6, 26.5)$	$i = 24.4$	31	<i>HST</i> ACS WFC, Program 9919
RX J1053.7+5735	Sloan (i-z)	1.00 ± 0.33	$\sim 1.0^a$	$(i,z) = (26.7, 24.8)$	$i = 24.5$	74	Subaru Suprime-Cam
RX J0848.9+4452	(F775W-F850LP)	0.91 ± 0.33	$\sim 1.0^a$	$(i,z) = (27.4, 27.3)$	$i = 25.1$	60	<i>HST</i> ACS WFC, Program 9919

NOTE. — Columns: (1) Cluster name (2) Optical colors used to create the color-magnitude diagram for the cluster (3) Mean color and the 3σ spread of cluster red sequence (CRS) galaxies determined by fitting a single component Gaussian profile to the color distribution of cluster red galaxies. See § 4.1 for details. (4) The expected observed color of CRS galaxies, as estimated from Fukugita et al. (1995) for E0 galaxies (5) The 3σ limiting optical magnitude of the images in the specified bandpass (6) Observed magnitude of an L^* galaxy at the cluster redshift. See § 4.1 for details on L^* . (7) Number of CRS galaxies brighter than L^* (8) Origin of the survey images, which includes the Sloan Digital Sky Survey Data Release 6 (SDSS DR6; Adelman-McCarthy et al. 2008), the *Chandra* Multi-wavelength Project (ChaMP; Green et al. 2004), the Astrophysical Research Consortium (ARC) 3.5m Telescope at Apache Point Observatory, the Hubble Space Telescope Advanced Camera for Surveys (*HST* ACS) with Program ID, and the National Astronomical Observatory of Japan's 8.2m Subaru Telescope at Mauna Kea.

^a The expected (r-i) color of a passive galaxy at $z \sim 1.0$ is estimated from Figure 2 in Mei et al. (2006b). Using the stellar population models of Bruzual & Charlot (2003), these authors estimated the (F775W-F850LP) colors of passive ellipticals at $z \sim 1.0$, assuming solar metallicities and a stellar population age of 4 Gyr.

TABLE 5
RADIO SOURCES WITHIN 1 MPC OF CLUSTERS AT $z > 0.4$

No. (1)	Object (2)	In? (3)	α (4)	δ (5)	z (6)	mag (7)	($r-i$) (8)	($i-z$) (9)	CRS (10)	Radius (11)	$S_{1.4GHz}$ (12)	$P_{1.4GHz}$ (13)	F_X (14)	L_X (15)	Comments (16)
1	MS1621-R1	S	16:23:35.1	26:34:27.2	0.427 ^a	$r=19.36$	0.66	...	0.66 ± 0.10	0.042	14.0 ± 0.2	82.5 ± 1.2	< 5.6	< 3.7	
2	MS1621-R2	S	16:23:32.2	26:33:44.0	0.431 ^a	$r=20.48$	0.65	...	0.66 ± 0.10	0.337	8.3 ± 0.2	47.7 ± 1.2	< 3.3	< 2.2	
3	MS1621-R3	NP	16:23:31.0	26:34:07.0	...	$r > 22.2$	0.66 ± 0.10	0.298	3.5 ± 0.2	...	< 3.6	...	
4	MS1621-R4	S	16:23:47.3	26:34:33.0	0.426 ^a	$r=18.91$	0.77	...	0.66 ± 0.10	1.012	2.2 ± 0.2	12.9 ± 1.2	< 8.9	< 5.8	
5	RXJ1221-R1*	P	12:21:25.7	49:18:34.2	...	$r=21.94$	1.27	...	1.27 ± 0.27	0.055	13.70 ± 0.09	(253.7 ± 1.6)	< 2.6	(< 5.7)	
6	RXJ1221-R2	S	12:21:29.2	49:18:16.1	0.6998 ^b	$r=21.26$	1.32	...	1.27 ± 0.27	0.224	13.41 ± 0.07	248.1 ± 1.6	< 1.9	< 4.1	
7	RXJ1221-R3	NP	12:21:20.2	49:18:46.0	...	$r=21.10$	0.15	...	1.27 ± 0.27	0.451	1.1 ± 0.06	...	94.7 ± 4.2	...	RXJ1221-X1 (Source 7) in Table 11
8	RXJ1221-R4	P	12:21:31.1	49:16:53.9	...	$r=22.13$	1.32	...	1.27 ± 0.27	0.768	0.5 ± 0.07	(9.1 ± 1.4)	< 1.3	(< 2.8)	
9	RXJ2302-R1*	S	23:02:48.1	08:43:50.8	0.722 ^c	$r=21.29$	1.41	...	1.31 ± 0.27	0.027	17.88 ± 0.15	355.8 ± 2.9	< 2.7	< 6.3	
10	RXJ1113-R1	NP	11:13:09.7	-26:16:10.1	...	$r=20.56$	1.05	...	1.41 ± 0.24	0.488	0.50 ± 0.03	...	< 1.2	...	
11	RXJ1350-R1	P	13:50:59.6	60:06:09.6	...	$i=20.40$	0.98	...	1.12 ± 0.21	0.784	5.56 ± 0.05	(138.8 ± 1.3)	< 1.4	(< 4.2)	
12	RXJ1350-R2	P	13:50:50.1	60:08:03.2	...	$i=21.49$	1.01	...	1.12 ± 0.21	0.409	0.96 ± 0.05	(23.9 ± 1.3)	3.1 ± 1.2	(7.7 ± 3.9)	RXJ1350-X7 (Source 31) in Table 11
13	RXJ1350-R3	P	13:50:41.9	60:07:15.2	...	$i=21.13$	1.10	...	1.12 ± 0.21	0.357	0.60 ± 0.05	(14.9 ± 1.3)	< 1.2	(< 3.8)	
14	RXJ1350-R4	NP	13:50:45.7	60:05:53.9	...	$i=23.16$	1.10	...	1.12 ± 0.21	0.596	0.24 ± 0.05	(6.0 ± 1.3)	< 1.7	(< 5.1)	
15	RXJ1716-R1	S	17:16:36.9	67:08:30.4	0.7947 ^d	$i=21.15$	1.22	...	1.30 ± 0.27	0.533	297 ± 12	$7.7 \pm 0.3 \times 10^3$	17.7 ± 2.5	46.0 ± 6.6	RXJ1716-X2 (Source 35) in Table 11
16	RXJ1716-R2*	S	17:16:48.8	67:08:21.9	0.8256 ^e	$i=19.36$	1.36	...	1.30 ± 0.27	0.011	5.02 ± 0.06	130.4 ± 1.5	< 7.1	< 22.3	
17	RXJ1716-R3	NS	17:16:51.7	67:08:53.5	2.067 ^d	$r > 24.3$	1.30 ± 0.27	0.260	2.08 ± 0.06	465.5 ± 13.4	27.1 ± 2.8	606.5 ± 62.7	RXJ1716-X1 (Source 34) in Table 11
18	RXJ1716-R4	S	17:16:56.8	67:09:03.7	0.8009 ^e	$i=22.55$	1.34	...	1.30 ± 0.27	0.461	0.75 ± 0.06	19.0 ± 1.5	< 0.6	< 1.9	
19	RXJ1415-R1*	S	14:15:11.2	36:12:04.2	1.01 ^c	$i=21.98$...	1.01	0.94 ± 0.15	0.012	3.15 ± 0.14	137.7 ± 5.9	< 10.0	< 54.1	
20	RXJ1415-R2	P	14:15:08.6	36:14:44.0	...	$i=23.78$...	0.74	0.94 ± 0.15	0.425	0.15 ± 0.02	(6.5 ± 0.8)	< 0.5	(< 2.6)	
21	RXJ1053-R1	NS	10:53:51.1	57:35:27.9	0.391 ^g	$i=21.10$...	0.43	1.00 ± 0.33	0.756	0.22 ± 0.02	1.1 ± 0.1	< 0.8	< 0.4	
22	RXJ1053-R2	NS	10:53:30.8	57:33:49.0	0.420 ^g	$i=24.56$...	0.65	1.00 ± 0.33	0.938	0.09 ± 0.02	0.5 ± 0.1	< 1.6	< 0.9	
23	RXJ1053-R3	NP	10:53:27.1	57:34:28.7	...	$i=23.56$...	0.33	1.00 ± 0.33	0.933	0.09 ± 0.02	...	4.6 ± 0.8	...	RXJ1053-X4 (Source 68) in Table 11
24	RXJ1053-R4*	S	10:53:40.0	57:35:17.5	1.135 ^f	$i=21.64$...	1.11	1.00 ± 0.33	0.015	0.09 ± 0.02	5.1 ± 1.2	< 3.2	< 23.3	
25	RXJ1053-R5	NS	10:53:28.9	57:35:35.6	0.741 ^h	$i=20.09$...	0.57	1.00 ± 0.33	0.751	0.08 ± 0.02	1.7 ± 0.04	< 0.9	< 1.9	
26	RXJ1053-R6	S	10:53:46.9	57:35:10.5	1.130 ^f	$i=21.89$...	1.13	1.00 ± 0.33	0.462	0.08 ± 0.02	4.5 ± 1.1	< 1.2	< 8.6	

NOTE. — Only radio sources at $P_{1.4GHz} \geq 5 \times 10^{23}$ W Hz⁻¹ at the cluster redshift are included in this table. Columns: (1) Object number (2) Radio galaxy name with brightest cluster galaxies (BCGs) identified with an asterisk. No radio galaxy was detected at $P_{1.4GHz} \geq 3 \times 10^{23}$ W Hz⁻¹ in MS2053 nor RXJ0152. (3) Cluster membership is identified as follows: S = spectroscopically-confirmed cluster member; NS = non-cluster member based on spectroscopy; P = probable cluster member based on photometry, which places the host galaxy on the CRS; NP = probable non-cluster based on either being a blank field, host galaxy at $L \geq L^*$, and/or bluer than the CRS. See §4.2 for details. (4-5) RA/DEC of the radio source (6) Object z with references listed below (7) Observed Sloan r -band or i -band magnitude (8) Observed ($r-i$) or (9) ($i-z$) colors (10) Mean color of $L \geq L^*$ CRS galaxy and the corresponding 3σ spread in color. See §4.1 for details. (11) Projected radial distance in Mpc from the cluster X-ray emission centroid (12) Observed 1.4 GHz radio flux density in mJy (13) 1.4 GHz radio power in units of 10^{23} W Hz⁻¹ at the known redshift, or at the cluster redshift if the source redshift is unknown (enclosed in parentheses) (14) Observed X-ray flux (0.3-8.0 keV) in units of 10^{-15} erg cm⁻² s⁻¹, assuming a power-law spectrum with $\Gamma=1.7$ ($N_E \propto E^{-\Gamma}$). See § 3.1 for details. (15) Rest-frame X-ray luminosity (0.3-8.0 keV) or limit in units of 10^{42} erg s⁻¹ at the source redshift, or at the cluster redshift if the source redshift is unknown (enclosed in parentheses). (16) Comments. References for source redshifts listed in Column 5: (a) Stocke et al. (1999) (b) Mullis et al. (2003) (c) Perlman et al. (2002) (d) Eckart et al. (2006) (e) Henry et al. (1997) (f) Hashimoto et al. (2005) (g) Zappacosta et al. (2005) (h) Hasinger et al. (1998)

TABLE 6
 CLUSTER XPSs WITHIN 1 MPC OF CLUSTERS AT $z > 0.4$

No. (1)	Object (2)	In? (3)	α (4)	δ (5)	z (6)	Net Counts (7)	F_X (8)	L_X (9)	R (10)	m (11)	Color (12)	$P_{1.4GHz}$ (13)
35 (A)	RXJ1716-X2	XC	17:16:37.0	+67:08:29.3	0.795 ^d	69.8 \pm 10.0	17.7 \pm 2.5	44.1 \pm 6.2	0.527	r=22.36	(r-i)=1.22	7.7e3 \pm 0.3e3
Comments: CXOSEXSI/CXOMP J171636.9+670829; RXJ1716-R1; [O II]; strong Ca HK; D4000; very strong [O III]												
40 (B)	RXJ1716-X9	XC	17:16:37.8	+67:07:30.8	0.8044 ^d	16.1 \pm 5.5	4.4 \pm 1.5	11.4 \pm 3.9	0.630	r=22.60	(r-i)=1.31	<4.2
Comments: CXOSEXSI/CXOMP J171637.6+670730; Source 33 from Table 1 of Gioia et al. (1999); only Ca H&K detected												
44 (C)	RXJ1716-X13	XC	17:17:03.9	+67:08:59.7	0.813 ^a	8.3 \pm 4.4	2.0 \pm 1.0	5.2 \pm 2.6	0.714	r=21.81	(r-i)=1.12	<4.2
Comments: CXOSEXSI J171703.8+670900, very weak [O II], Ca HK; CXOMP J171703.8+670859; Object 9 from Table 1 of Gioia et al. (1999)												
62 (D)	RXJ0910-X11	XB	09:10:42.7	+54:20:36.4	1.108 ^a	14.1 \pm 5.1	1.6 \pm 0.6	8.6 \pm 3.2	0.732	i=22.04	(i-z)=0.49	<11.3
Comments: CXOMP J091042.7+542036; CXOSEXSI J091042.7+542034, weak [O II], elliptical host; Object 66 from Table 6 of Martel et al. (2007)												
66 (E)	RXJ0910-X16	XC	09:10:48.3	+54:22:29.6	1.1108 ^g	8.7 \pm 4.7	1.0 \pm 0.5	5.4 \pm 2.7	0.315	i=23.88	(i-z)=1.00	<11.3
Comments: CXOMP J091048.3+542229; CXOSEXSI J091048.3+542228; Object 023 from Table 1 of Stanford et al. (2002) Object 51 from Table 6 of Martel et al. (2007)												
80 (F)	RXJ0849-X4	XC	08:49:05.3	+44:52:04.0	1.266 ^a	65.0 \pm 9.6	4.5 \pm 0.7	32.5 \pm 4.8	0.597	i=24.00	(i-z)=0.91	<13.0
Comments: CXOMP J084905.2+445202; CXOSEXSI J084905.3+445203 with weak [O II], weak Ca HK; Object 60 from Table 5 of Martel et al. (2007)												
83 (G)	RXJ0849-X8	XC	08:49:04.0	+44:50:24.8	1.276 ^a	16.9 \pm 6.2	1.1 \pm 0.4	8.2 \pm 2.9	0.872	i=23.22	(i-z)=1.02	<13.0
Comments: CXOMP J084904.0+445024; CXOSEXSI J084903.9+445023 with [O II] emission; Object 156 from Tables 1-2 of Stern et al. (2002); Object 67 from Table 5 of Martel et al. (2007)												

NOTE. — Comments for each source, including alternative names of the XPS from other X-ray surveys and optical spectral line identifications, follow each source's entry.

Columns: (1) Source number (and letter identifier in parentheses) (2) Cluster X-ray point source ID (3) Classification tag as follows: XC = spectroscopically-confirmed cluster member on the CRS; XB = spectroscopically-confirmed cluster member bluer than the CRS; (4-5) J2000 RA and DEC from CIAO *wavdetect* routine; (6) Source redshift with references listed below; (7) Net X-ray (0.3-8.0 keV) counts; (8-9) X-ray (0.3-8.0 keV) flux in units of 10^{-15} erg cm $^{-2}$ s $^{-1}$ and corresponding luminosity in units of 10^{42} erg s $^{-1}$ at the source redshift or at the cluster redshift, if the source redshift is unknown; (10) Projected distance, R, from the cluster X-ray emission centroid in Mpc; (11-12) Apparent optical magnitude and color; (13) 1.4 GHz Radio power or limit of the X-ray source in units of 10^{23} W Hz $^{-1}$; The following notation is used in this column: BLAGN = Broadline AGN, ELG = Emission-line galaxy. References for source redshifts: (a) Eckart et al. (2006) (b) Silverman et al. (2005) (c) Kim et al. (2006) (d) Gioia et al. (1999) (e) Demarco et al. (2005) (f) Martel et al. (2007) (g) Stanford et al. (2002) (h) Hasinger et al. (1998) (i) Mateos et al. (2005) (j) Stern et al. (2002)

TABLE 7
CUMULATIVE RADIAL DISTRIBUTION OF CLUSTER RADIO GALAXIES COMPARED TO CRS GALAXIES

Redshift Bin (1)	With BCGs? (2)	K-S D-statistic (3)	Probability (4)	Significance (5)
0.2 < z < 0.4	Y	0.43	1.1×10^{-8}	5.7σ
	N	0.36	3.3×10^{-6}	4.7σ
0.4 < z < 0.8	Y	0.44	4.5×10^{-9}	5.9σ
	N	0.33	2.7×10^{-5}	4.2σ
0.8 < z < 1.1	Y	0.31	1.0×10^{-4}	3.9σ
	N	0.32	5.4×10^{-5}	4.0σ

NOTE. — Columns: (1) Cluster redshift bin (2) Are the BCGs included in the cumulative radial distribution function? (3) Two-sided Komolgorov-Smirnov (K-S) test D-statistic, which is a measure of the maximum difference between the radio galaxy cumulative radial distribution function compared to the CRS galaxy distribution. (4) Two-sided K-S test probability that the distributions are drawn from the same parent distribution. (5) Significance level of the probability.

TABLE 8
“ROAD TO COMA” CLUSTER RADIO LUMINOSITY FUNCTION

Redshift (1)	N_{CRS} (2)	$\text{Log}(P_{1.4GHz})$ Bin (3)	N_{Radio} (4)	$\text{Log}(N_{Radio}/N_{CRS})$ (5)
0.2 < z < 0.4	665	23.6–24.0	5	-2.12 ± 0.16
		24.0–24.4	6	-2.04 ± 0.15
		24.4–24.8	5	-2.12 ± 0.16
		24.8–25.2	1	-2.82 ± 0.30
		25.2–26.0	0	< -2.8
		26.0–27.0	0	< -2.8
0.4 < z < 1.1	443	23.6–24.0	4	-2.04 ± 0.18
		24.0–24.4	4	-2.04 ± 0.18
		24.4–24.8	1	-2.65 ± 0.30
		24.8–25.2	4	-2.04 ± 0.18
		25.2–26.0	3	-2.17 ± 0.20
		26.0–27.0	1	-2.65 ± 0.30

NOTE. — Columns: (1) Cluster redshift bin (2) Number of $L \geq L^*$ CRS galaxies within 1 Mpc of the cluster center (3) $\text{Log}(P_{1.4GHz})$ bin in units of $W \text{ Hz}^{-1}$ (4) Number of radio sources detected in the specified $\text{log}(P_{1.4GHz})$ bin (5) Log of the fraction of CRS galaxies that host radio sources in the specified $\text{log}(P_{1.4GHz})$ bin. See §4.1 for the details on the CRS galaxies number calculation. Quoted errors are one-sided Poisson errors, using Gehrels (1986) approximation.

TABLE 9
DIFFERENCES IN THE EXPECTED VS. DETECTED CLUSTER RADIO GALAXY COUNTS

Log(P) (1)	Surveys (2)	N_{exp} (3)	N_{det} (4)	% Probability (5)
23.6-25.0	Paper I vs. This work	11.3	10	70
23.6-25.0	Ledlow & Owen (1996) vs. Paper I	16.2	15	66
23.6-25.0	Ledlow & Owen (1996) vs. This work	10.8	8	85
24.0-25.0*	Stocke et al. (1999) vs. Paper I	7.6	10	23
24.0-25.0*	Stocke et al. (1999) vs. This work	5.0	5	56
>25.0	Paper I vs. This work	0	7	0**
>25.0	Ledlow & Owen (1996) vs. This work	2.2	6	2
>25.0	Stocke et al. (1999) vs. This work	0.3	6	7×10^{-5}

NOTE. — Columns: (1) $\log(P_{1.4GHz})$ in $W Hz^{-1}$ (2) Surveys that are being compared (3) Number of expected radio galaxies based on the first survey listed in Column 2 (4) Number of detected radio galaxies in the second survey in Column 2 (5) Cumulative binomial probability (%) of detecting $\geq N_{det}$ radio galaxies in the second survey

* The sample of cluster radio galaxies from Stocke et al. (1999) is incomplete at $\log(P_{1.4GHz}) < 24 W Hz^{-1}$.

** Based on our detected number of $\log(P_{1.4GHz}) > 25 W Hz^{-1}$ radio galaxies at $0.4 < z < 1.2$, we expect to detect 10.5 radio sources at $\log(P_{1.4GHz}) > 25 W Hz^{-1}$ in our $0.2 < z < 0.4$ cluster sample, but we detected none. The binomial probability of detecting no source is 0.003%.

TABLE 10
NUMBER OF EXPECTED VS. DETECTED X-RAY POINT SOURCES

Redshift Bin (1)	$N_{clusters}$ (2)	Area (3)	Cut-Off Limit (4)	$N_{detected}$ (5)	N_{bgd} (6)	Excess (7)
0.2–0.4	11	0.165	$L_{0.3-8.0keV} \geq 5 \times 10^{42}$	22	19.9 ± 6.8	0.3σ
...	$L_{0.3-8.0keV} \geq 1 \times 10^{42}$	105	103.8 ± 23.1	0.05σ
0.4–0.8	5	0.028	$L_{0.3-8.0keV} \geq 5 \times 10^{42}$	24	23.6 ± 6.8	0.06σ
0.8–1.26	6	0.022	$L_{0.3-8.0keV} \geq 5 \times 10^{42}$	62	44.3 ± 11.1	1.6σ

NOTE. — Columns: (1) Redshift range (2) Number of clusters in the given redshift bin (3) Total area surveyed in square degrees (4) Limiting luminosity for an individual source (0.3–8.0 keV) in $erg s^{-1}$ at the cluster redshift. (5) Total number of detected XPSs in the cluster observations within 1 Mpc of the cluster center (6) Number of expected background XPSs above the specific limit listed in Column 4. The quoted error is the contribution from statistical fluctuations and $\approx 20\%$ due to cosmic variance in the estimated background counts added in quadrature. (7) Statistical excess of detected XPSs above the expected XPS background from Column 6 in the units of σ . Note that RXJ0152 is not included in this specific analysis.

TABLE 11
XPSs WITHIN 1 MPC OF CLUSTERS AT $z > 0.4$

No. (1)	Object (2)	Cl Src? (3)	RA DEC (4)	z (5)	Net Counts (6)	F_X (7)	L_X (8)	R (9)	m (10)	Color (11)	$P_{1.4GHz}$ (12)	Comments (13)
1	MS1621-X1	BG	16:23:43.8 +26:32:44.7	0.659 ^a	430.3±22.5	171.5±9.0	276.1±14.5	0.826	r=19.52	(r-i)=0.00	<0.8	CXOSEXSI J162343.7+263244, BLAGN
2	MS1621-X2	BG	16:23:27.3 +26:32:07.3	1.438 ^a	59.5±9.1	23.6±3.6	231.8±35.4	0.959	r=20.86	(r-i)=0.55	<0.8	CXOSEXSI J162327.2+263207, BLAGN
3	MS1621-X3	CRS2	16:23:36.1 +26:36:52.6	...	40.5±7.7	15.3±2.9	9.0±1.7	0.849	r=22.8	(r-i)=0.54	<0.8	CXOSEXSI J162335.9+263652
4	MS1621-X4	BG	16:23:45.9 +26:33:35.0	1.283 ^a	22.7±6.4	9.0±2.6	68.0±19.6	0.826	r>22.2	...	<0.8	CXOSEXSI J162345.7+263335, ELG
5	MS2053-X1	BG	20:56:22.3 -04:40:07.3	0.641 ^a	114.2±12.1	37.3±3.9	56.3±5.9	0.918	r=21.21	(r-i)=0.51	<2.2	CXOSEXSI J205622.2-044005, ELG
6	MS2053-X2	FG	20:56:24.8 -04:35:35.4	0.260 ^a	28.0±6.9	9.9±2.5	1.9±0.5	0.945	r=19.48	(r-i)=0.55	<2.2	CXOSEXSI J205624.7-043533, ELG
7	RXJ1221-X1	BLU	12:21:20.1 +49:18:45.8	...	598.5±26.4	94.7±4.2	175.4±7.7	0.462	r=21.10	(r-i)=0.15	20.7±1.2	CXOMP J122120.1+491846, unlikely cluster member based on radio & optical color; Also RXJ1221-R3 (Source 7 in Table 5)
8	RXJ1221-X2	BLU2	12:21:29.0 +49:16:45.4	...	19.7±5.9	3.5±1.0	6.5±1.9	0.747	r=24.19	(r-i)=0.94	<2.0	CXOMP J122129.0+491645
9	RXJ1221-X3	CRS	12:21:30.8 +49:17:58.8	...	16.8±5.9	2.9±1.0	5.3±1.9	0.365	r=22.87	(r-i)=1.20	<2.0	V 1221+4918, Source 5 from Table 2 of Branchesi et al. (2007)
10	RXJ2302-X1	BG	23:02:46.1 +08:45:22.8	1.944 ^b	441.6±22.7	156.1±8.0	3043.6±156.0	0.684	r=19.08	(r-i)=0.52	<3.5	WARP J2302.7+0845; CX- OMP J230246.0+084523, BLAGN

NOTE. — Table 11 is published in its entirety in the electronic edition of the Astrophysical Journal. A portion is shown here for guidance regarding its form and content. Columns: (1) Source number (and letter identifier in parentheses) (2) Cluster X-ray point source ID (3) Classification tag as follows: XC = spectroscopically-confirmed cluster member on the CRS; XB = spectroscopically-confirmed cluster member bluer than the CRS; FG = spectroscopically-confirmed foreground non-cluster source; BG = spectroscopically-confirmed background non-cluster source; CRS = source host galaxy with CRS colors at an unknown redshift and with $L \geq L^*$ if located at the cluster redshift; CRS2 = similar to CRS but with $L < L^*$ host galaxy; BLU = XPS hosted in $L \geq L^*$ host galaxy with colors bluer than typical CRS galaxies and with unknown redshift; BLU2 = similar to BLU, but with $L < L^*$ host galaxy at the cluster redshift; BLU3 = similar to BLU, but with $L \geq L_{BCG}$ host galaxy; NO = No optical counterpart is detected in one or both optical images; NP = No photometric data in one or both optical images; (4) J2000 RA and DEC from CIAO *wavdetect* routine; (5) Source redshift with references listed below; (6) Net X-ray (0.3-8.0 keV) counts; (7-8) X-ray (0.3-8.0 keV) flux in units of 10^{-15} erg cm⁻² s⁻¹ and X-ray (0.3-8.0 keV) luminosity in units of 10^{42} erg s⁻¹ at the source redshift or at the cluster redshift, if the source redshift is unknown; (9) Projected distance, R, from the cluster X-ray emission centroid in Mpc; (10-11) Optical magnitude and color; (12) 1.4 GHz radio power or limit of the X-ray source in units of 10^{23} W Hz⁻¹; (13) Comments, including alternative names of the XPS from other X-ray surveys and optical spectral line identifications. The following notation is used in this column: BLAGN = Broadline AGN, ELG = Emission-line galaxy per SEXSI identification by Eckart et al. (2006). References for source redshifts: (a) Eckart et al. (2006) (b) Silverman et al. (2005) (c) Kim et al. (2006) (d) Gioia et al. (1999) (e) Demarco et al. (2005) (f) Martel et al. (2007) (g) Stanford et al. (2002) (h) Hasinger et al. (1998) (i) Mateos et al. (2005) (j) Stern et al. (2002)